

TITANIUM DIOXIDE/ SILICON OXYCARBIDE HYBRID POLYMER DERIVED  
CERAMIC AS HIGH ENERGY & POWER LITHIUM ION BATTERY ANODE MATERIAL

by

SAKSHAM PAHWA

B.Tech, National Institute of Technology Karnataka, India 2013

A THESIS

submitted in partial fulfillment of the requirements for the degree

MASTER OF SCIENCE

Department of Mechanical and Nuclear Engineering  
College of Engineering

KANSAS STATE UNIVERSITY  
Manhattan, Kansas

2016

Approved by:

Major Professor  
Dr Kevin Lease

Co - major Professor  
Dr Gurpreet Singh

# **Copyright**

SAKSHAM PAHWA

2016

## Abstract

Energy has always been one of the most important factors in any type of human or industrial endeavor. Clean energy and alternative energy sources are slowly but steadily replacing fossil fuels, the over-dependence on which have led to many environmental and economic troubles over the past century. The main challenge that needs to be addressed in switching to clean energy is storing it for use in the electrical grid and transportation systems. Lithium ion batteries are currently one of the most promising energy storage devices and tremendous amount of research is being done in high capacity anode and cathode materials, and better electrolytes and battery packs as well, leading to overall high efficiency and capacity energy storage systems. Polymer derived ceramics (PDCs) are a special class of ceramics, usually used in high temperature applications, but some silicon based PDCs have demonstrated good electrochemical properties in lithium ion batteries. The goal of this research is to explore a special hybrid ceramic of titanium dioxide ( $\text{TiO}_2$ ) and silicon oxy carbide (SiOC) ceramic derived from 1,3,5,7 - tetravinyl - 1,3,5,7 - tetramethylcyclotetrasiloxane (TTCS) polymer for use in lithium ion batteries and investigate the source of its properties which might make the ceramic particularly useful in some highly specialized energy storage applications.

# Table of Contents

List of Figures .....	vi
List of Tables .....	ix
Acknowledgements.....	x
Dedication .....	xi
Chapter 1 - Introduction.....	1
1.1 Motivation.....	1
1.2 Overview of thesis .....	7
References .....	8
Chapter 2 - Literature Review.....	11
2.1 Lithium ion batteries.....	11
2.1.1 Cathode .....	15
2.1.2 Anode.....	18
2.1.3 Electrolyte .....	21
2.3 Polymer derived ceramics.....	22
2.3.1 Introduction.....	22
2.3.2 Silicon oxy-carbide .....	28
References .....	31
Chapter 3 - Processing of TiO <sub>2</sub> - SiOC.....	41
3.1 Introduction.....	41
3.2 Experimental Procedure.....	42
References .....	49
Chapter 4 - Characterization of TiO <sub>2</sub> – SiOC .....	51
4.1 Scanning Electron Microscopy .....	51
4.2 Transmission Electron Microscopy .....	53
4.3 Fourier Transform infrared spectroscopy .....	56
4.4 X- Ray Diffraction .....	58
4.5 Raman Spectroscopy.....	59
References .....	62
Chapter 5 - Electrochemical Performance of TiO <sub>2</sub> – SiOC .....	64

References .....	70
Chapter 6 - Conclusion and Future Work .....	72

## List of Figures

Figure 1 World Energy consumption by fuel (quadrillion btu) [1] .....	1
Figure 2 Evolution of the HEV market [2] .....	2
Figure 3 Evolution of the LIB sale in consumer electronic and HEV market [2] .....	3
Figure 4 Battery specific power vs specific energy consumption [4].....	4
Figure 5 Working mechanism for primary and secondary batteries [7] .....	5
Figure 6. Theoretical specific energy of various rechargeable battery systems vs practical specific energies [13] .....	6
Figure 7 Constant current charge – discharge cycles (1-3) of the SiOC – TiO <sub>2</sub> hybrid anodes [19] .....	7
Figure 8 Schematic illustration of the LiCoO <sub>2</sub> /C battery [2].....	11
Figure 9 Open circuit diagram of an electrolyte with cathode and anode potentials [1] .....	13
Figure 10 Voltage versus capacity of several electrode materials in LiPF <sub>6</sub> .....	14
Figure 11 A schematic representation of the different reaction mechanisms observed in electrode materials for lithium batteries [10].....	14
Figure 12 Performance criteria of evaluating cathode materials, LCO, NMC,NCA = layered, LMO = spinel, LFP = olivine [17] .....	15
Figure 13 Comparison of operating voltage and practical capacity of various cathode materials presently used in Li-ion batteries [67] .....	16
Figure 14 Principle of operation of the first commercialized lithium-ion batteries [10].....	17
Figure 15 Graphite and LTO intercalation anodes .....	18
Figure 16 Specific capacities and capacity densities for selected alloying reactions [10] .....	19
Figure 17 Alloying reaction in a Silicon anode [39].....	20
Figure 18 Intercalation and conversion reaction mechanisms [68] .....	21
Figure 19 Common electrolyte solvents [68].....	22
Figure 20 General chemical formula for PDCs [55].....	23
Figure 21 Showing SiOC and SiCN precursors and ceramics [55] .....	23
Figure 22 Polymer to ceramic transformation [52].....	24
Figure 23 Microstructural model for SiCN ceramic [52] .....	25
Figure 24 EF-TEM image of a carbon-rich SiCO ceramic showing “free” carbon phase [52] ....	25

Figure 25 Tunable engineering properties for PDCs- [44] .....	26
Figure 26 Temperature dependence of electrical resistance of SiCO and SiBCO ceramics annealed at 1300°C for different times [45].....	27
Figure 27 Selected applications of PDCs [52].....	28
Figure 28 TTCS chemical structure .....	29
Figure 29 Schematic showing inter-domain boundaries containing graphene layers with mixed Si-C-O bonds [52].....	29
Figure 30 SEM image of the Si-O-C composite under a hydrogen atmosphere [57].....	30
Figure 31 The insertion and extraction of lithium into polymer-derived SiCO is hysteretic [66]	30
Figure 32 Showing capacity degradation in silicon oxy carbide [44] .....	31
Figure 33 Thermal decomposition methods for silicon-based polymers [5] .....	41
Figure 34 Showing the material put in for cross-linking .....	42
Figure 35 Showing the complete cross linking apparatus .....	43
Figure 36 Showing the input and output gas pipes in the cross linking apparatus .....	44
Figure 37 Crushed mixture to be put in for pyrolysis.....	44
Figure 38 Mixture being prepared to be put in the pyrolysis oven after weighing.....	45
Figure 39 Figure showing how the program for pyrolysis is set up .....	45
Figure 40 Final product obtained after pyrolysis.....	46
Figure 41 Ceramic boat after material removal after pyrolysis .....	46
Figure 42 Carbon black and binding agent for electrode coating.....	47
Figure 43 Mixing the pyrolyzed material with binder .....	48
Figure 44 Clamping the copper foil on the glass slate.....	48
Figure 45 Coating the copper foil using the doctor blade method.....	49
Figure 46 Screenshots of the SEM used during our analysis.....	51
Figure 47 Showing the SEM imaging of the sample .....	52
Figure 48 (a) SEM image of sample, (b) SEM image after cycling, (c) and (d) Proposed ceramic structure at 600° and 800° C[1].....	54
Figure 49 TEM images of – (a) TiO <sub>2</sub> only, (b) 10% sample, (c) 30% sample, (d) 50% sample .	55
Figure 50 Instruments used for FTIR.....	56
Figure 51 FTIR measurements of the different samples.....	57
Figure 52 Instruments for XRD .....	58

Figure 53 XRD plots of the samples.....	59
Figure 54 Raman spectroscopy of silicon oxy carbide .....	60
Figure 55 Raman plots of the three samples.....	61
Figure 56 Showing the first cycle charge and discharge of the batteries.....	64
Figure 57 Cycling efficiency of the 30% sample.....	65
Figure 58 showing the first cycle performance of the batteries.....	66
Figure 59 C-rate capability of the three anodes .....	67
Figure 60 Charge – discharge cycling of the 30% sample.....	67
Figure 61 Showing the electrochemical cycling and cycling efficiency of the batteries.....	68
Figure 62 Schematic showing domains of free carbon and micropore in SiOC ceramic [13] .....	68
Figure 63 Schematic representing the anode [11] - .....	69



## List of Tables

Table 1 Summary of electrochemical performance for two cycles .....	65
---	----

## **Acknowledgements**

I would like to express my gratitude to my co-advisors, Dr. Kevin Lease and Dr Gurpreet Singh, and Dr Hitesh Bindra for guiding me through this research and providing valuable inputs to improve my work . Financial support from National Science Foundation Grant number 1335862 is gratefully acknowledged.

I would also like to express my gratitude to my professors Dr Fenton, Dr White, Dr Eckels and Dr Dunn for their support and encouragement throughout my master's thesis. I would also like to thank Dr. Daniel Boyle, Dr. Charles Ye (KU), Dr. John Desper, Dr. Kenneth Klabunde, and Dr. Hongwang Wang for providing training and access to various characterization instruments. I am extremely thankful to my colleagues John Herrmann, Uriel Barerra, Nasim Rahmani and Lamuel David, for helping me with various academic, research as well as non- academic activities.

## **Dedication**

*This work is dedicated to my family and friends.*

# Chapter 1 - Introduction

## 1.1 Motivation

The world has been highly dependent on fossil fuels to generate energy ever since the industrial revolution, and with the increasing population and the tremendous rise in the number of automobiles and factories, these resources are depleting at a rate faster than experienced ever before in the human history. As such, governments and world populations have realized that there is an urgent need to find alternative sources of energy generation and storage to avoid the harmful effects of over-use of fossil fuels, which include, but are not limited to the depletion of these resources, global warming and pollution [1-3]. Figure 1 shows projected global energy consumption by fuel from the year 1990 to the year 2040 [1] and as seen, there is highest projected rise in renewable energy over the next 25 years, while the usage of fossil fuels is projected to reduce.

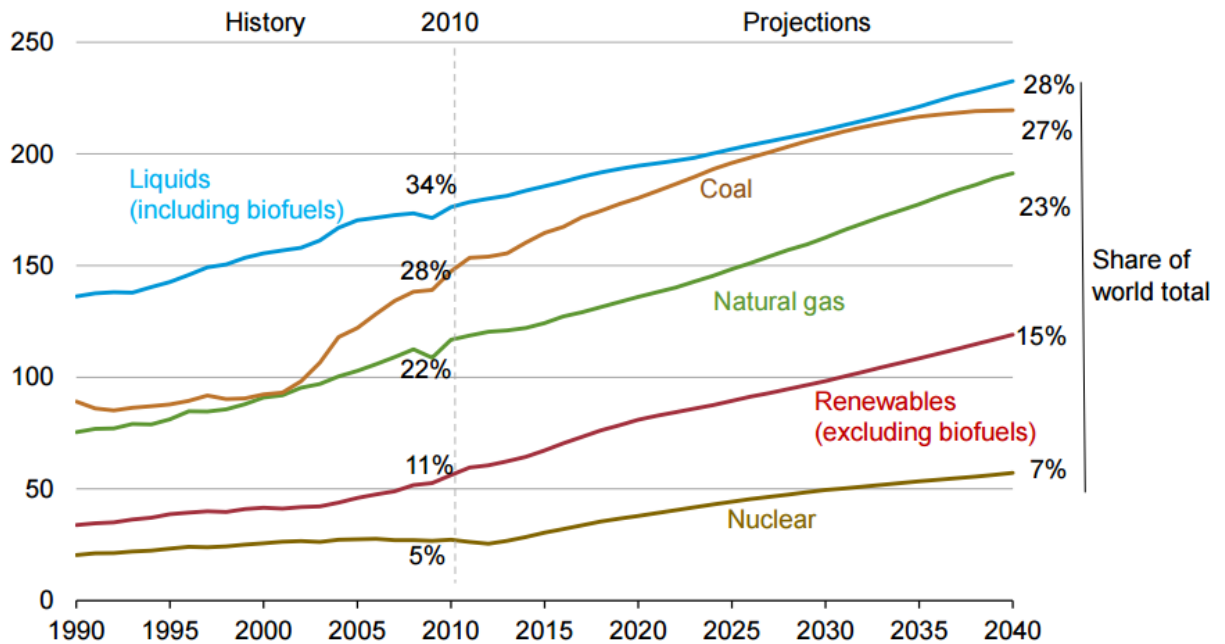


Figure 1 World Energy consumption by fuel (quadrillion btu) [1]

To address these issues, there have been tremendous amounts of research and investment in harnessing usable energy from renewable sources like wind, solar and geo-thermal. However, the common limitation for all these sources of energy is the energy storage capacity which is limited by battery technology.

Energy generation through hydro-electric, nuclear and the existing solar and wind energy sources has been transferred well into the existing power grid to satisfy the needs of our communities and industries. However, the major problem that needs to be addressed now is to utilize clean energy in our transportation systems. There have been many efforts in the past few years to make electric and hybrid electric vehicles (HEVs) mainstream and Figure 2 shows the projected evolution of the global hybrid electric vehicle market for the past decade [2].

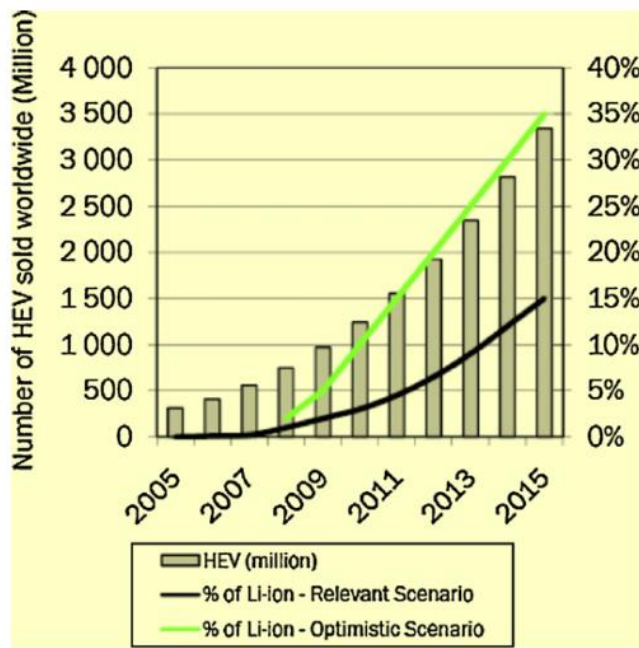
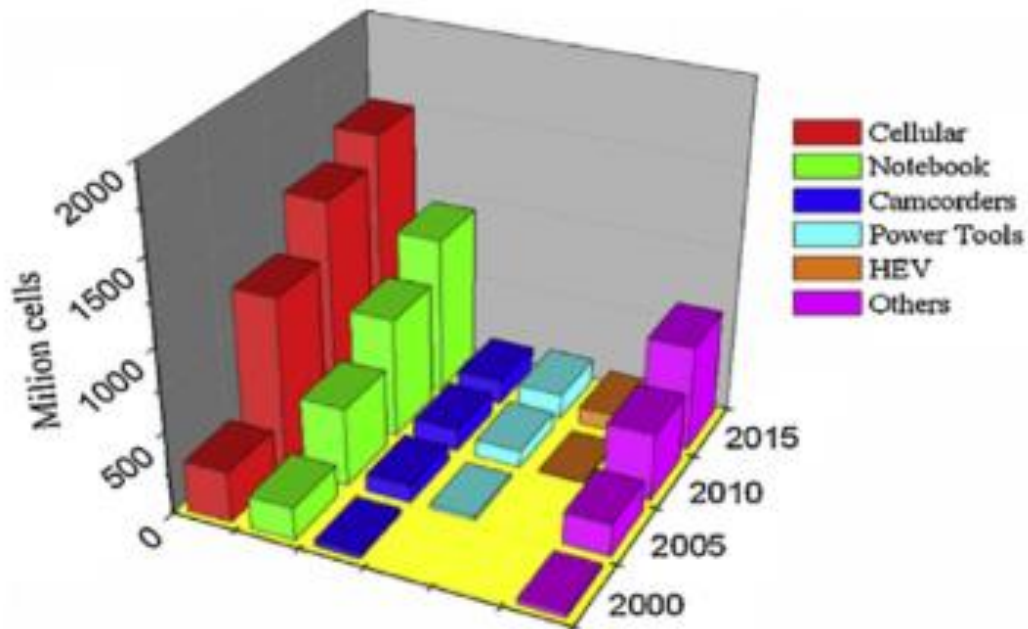


Figure 2 Evolution of the HEV market [2]

The primary requirement for locomotives is to store chemical energy in some form or the other, and convert it to usable forms of energy for conversion to kinetic energy when required. At present there have been quite some technologies that have been developed or are being researched to deliver similar performance as internal combustion engines, which might make use of alternate, cleaner fuels, or might use different approaches of energy storage and conversion altogether. Some of these include hydrogen fuel, fuel cells and batteries [2-3]. Each of the technologies have their own limitations, but Li-ion batteries seem to have raced past the other technologies mainly due to technological advancements in the consumer electronics segment, which enable technology transference to transportation systems as well. Figure 3 shows the evolution of the lithium ion battery consumer electronic and automobile markets between the years 2000 and 2015.



**Figure 3 Evolution of the LIB sale in consumer electronic and HEV market [2]**

Batteries have been used to run electric automobiles since the 1890s. However the lead acid batteries used in the earlier cars suffered from low gravimetric and volumetric energy densities and the developments in the IC engine technologies rendered them as inferior sources of energy for over a century. Lithium is the third lightest element and has the highest oxidation potential of all known elements and hence lithium batteries offer the best prospects for developing high energy and high power batteries to satisfy the future needs of electrified transportation. Figure 4 shows a comparison of the power and energy densities for different battery chemistries. It can be clearly observed that the lithium ion batteries exhibit the most superior gravimetric power and energy densities among all other chemistries.

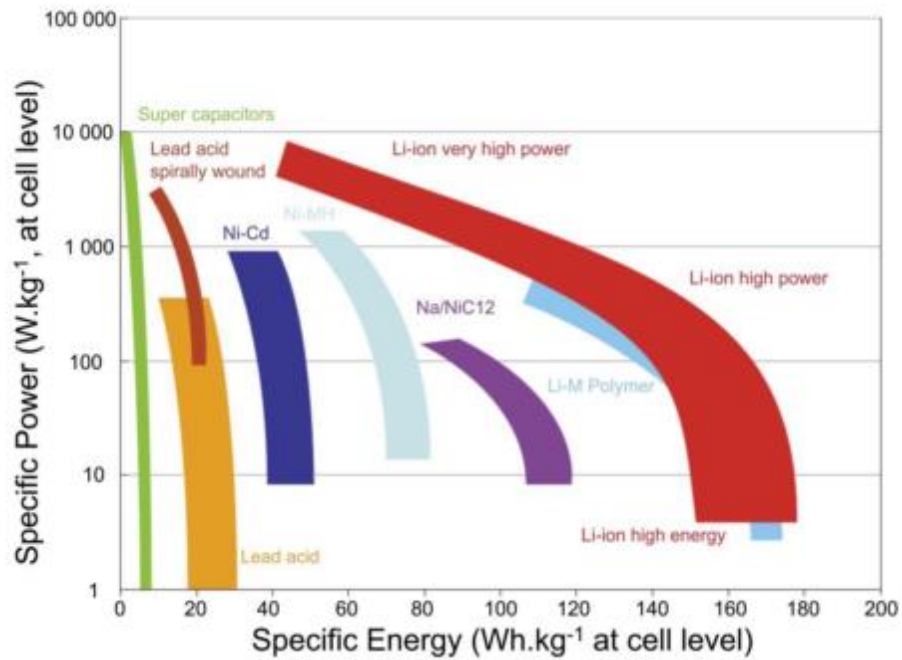


**Figure 4 Battery specific power vs specific energy consumption [4]**

Lithium ion batteries have high cell potential which allows them to store more energy per unit weight and volume compared to chemistries like lead acid, nickel cadmium or nickel metal hydride

[5-6]. Though they have their own limitations, they are better options to technologies like hydrogen fuel, or fuel cells, which need usage of expensive and rare materials like platinum and need heavy storage tanks to carry hydrogen on the vehicle.

Lithium ion batteries were invented in 1960 by Dr John Goodenough. The initial lithium ion batteries were based on the lithium sulphur chemistry, where the cathode was the lithium metal and the anode was made of sulphur. This battery could not be used in commercial applications due to inherent safety issues, like dendrite formation in the lithium cathode due to cycling over a period of time, which made it prone to short circuits and rendered it unsuitable for any kind of commercial use. Figure 5 shows schematically, the working mechanism for primary and secondary batteries.

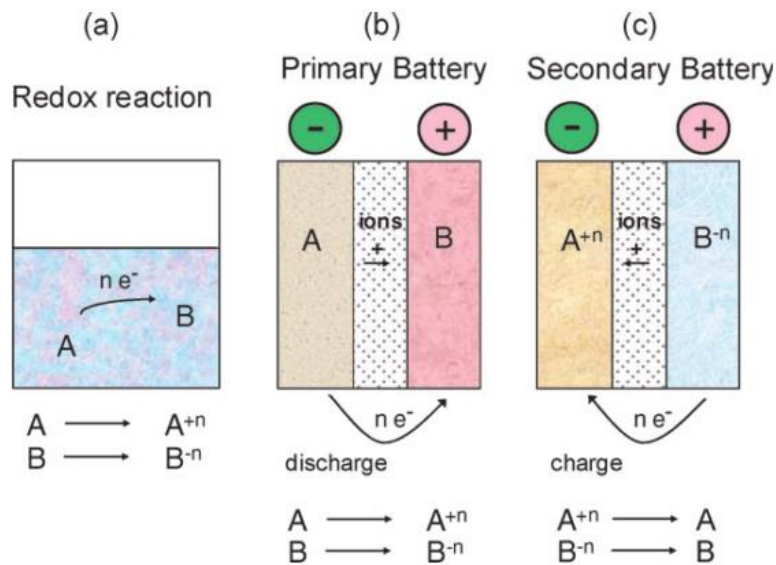


**Figure 5 Working mechanism for primary and secondary batteries [7]**

In 1991, Sony was able to successfully commercialize lithium ion batteries for portable devices by using the lithium cobalt oxide and graphite chemistry. The advancements in this technology since



then have led to the development of a number of types of lithium ion batteries having various chemistries and form factors, for a wide variety of applications from portable computers and smartphones to grid storage and now, electric and hybrid automobiles [7-15].

In order to satisfy the steadily growing energy needs and power demands of our energy-based society there is an urgent need to research suitable materials for next generation anodes, cathodes, as well as prospective electrolytes, with superior properties than existing materials. However, commercial production and a break-through in the development of high capacity cathode materials is considered to be less likely and research in anode materials seems to be the way forward [15-18]. Figure 6 compares the energy density of present lithium ion batteries to gasoline engines. Increasing the specific energy of lithium-ion cells requires anode and cathode materials with higher capacity and/or cell voltage. In this respect, several approaches are being adopted in attempts to enhance the performance of state- of-the-art lithium-ion batteries [13].

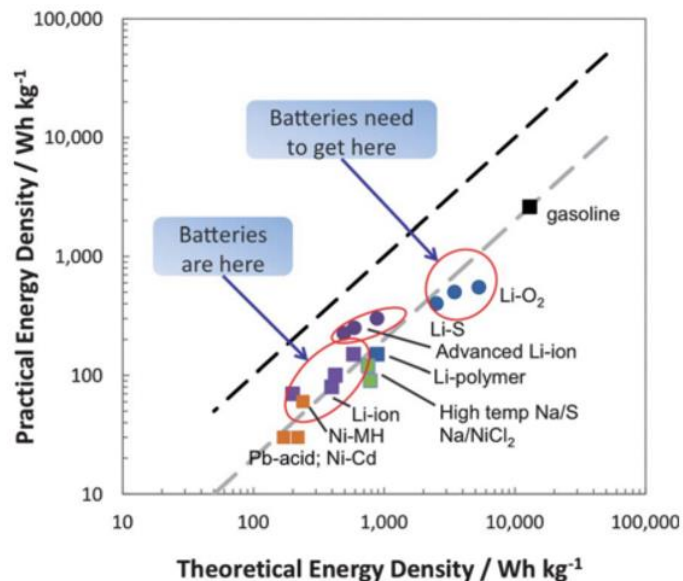


**Figure 6. Theoretical specific energy of various rechargeable battery systems vs practical specific energies [13]**

In this context, the objective of this thesis is the investigation of silicon oxycarbide/ TiO<sub>2</sub> nano-composite as a prospective anode material, which has been reported to have remarkable capacity as shown in Figure 7, C- rate capability and durability [19] and to explain the source of these properties.

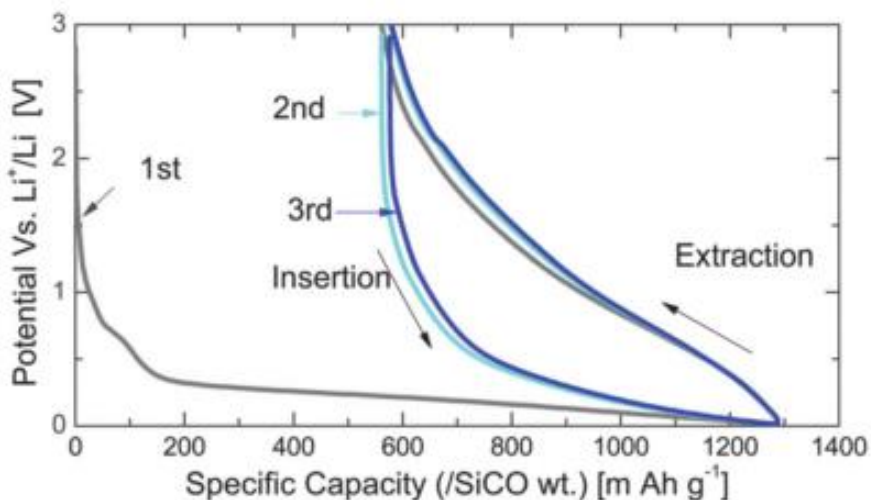


**Figure 7 Constant current charge – discharge cycles (1-3) of the SiOC – TiO<sub>2</sub> hybrid anodes [19]**

The composite is synthesized by means of a two-step cross-linking and pyrolysis process and characterized by means of various chemical and electrochemical techniques, the observations are presented and the reason for these properties is explained.

## 1.2 Overview of thesis

Chapter 1 introduces the reader to the objective of the thesis, highlights the motivation and gives an overview of the thesis.

Chapter 2 introduces the mechanism of Li ion batteries and includes the literature review of different battery components – anode, cathode and electrolyte materials. It also provides a

literature review of polymer derived ceramics (PDCs) including their structure and properties and their application in batteries.

Chapter 3 details the processing and synthesis of the carbon rich silicon oxy-carbide – titanium dioxide composite (TiO<sub>2</sub>– SiOC/C) ceramic and explains the reasons for its remarkable properties.

Chapter 4 details the chemical and physical characterization of the TiO<sub>2</sub> – SiOC/C composite.

Chapter 5 discusses the electrochemical performance of the composite material.

And Chapter 6 discussed the conclusion and future work to be done beyond this thesis.

## References

1. Adam Sieminski, International Energy Outlook, *Deloitte Oil and Gas Conference, U.S Energy Information Administration*, (2014).
2. Scrosati, B. & Garche, J. Lithium batteries: Status, prospects and future. *Journal of Power Sources* **195**, 2419-2430, doi:10.1016/j.jpowsour.2009.11.048 (2010).
3. Giridhar, P. *et al.* A review on lithium - Ion polymer electrolyte batteries. *Bulletin of Electrochemistry* **15**, 414-418 (1999).
4. R. Bhandavat, Z. Pei, G Singh, Polymer-derived ceramics as anode material for rechargeable Li-ion batteries: a review. *Nanomaterials and Energy* **1**, 324-327 (2012)
5. Choi, N.-S. *et al.* Challenges Facing Lithium Batteries and Electrical Double-Layer Capacitors. *Angewandte Chemie-International Edition* **51**, 9994-10024, doi:10.1002/anie.201201429 (2012).
6. Etacheri, V., Marom, R., Elazari, R., Salitra, G. & Aurbach, D. Challenges in the development of advanced Li-ion batteries: a review. *Energy & Environmental Science* **4**, 3243-3262, doi:10.1039/c1ee01598b (2011).
7. Rosa Palacin, M. Recent advances in rechargeable battery materials: a chemist's

- perspective. *Chemical Society Reviews* **38**, 2565-2575, doi:10.1039/b820555h (2009).
8. Goodenough, J. B. & Kim, Y. Challenges for Rechargeable Li Batteries. *Chemistry of Materials* **22**, 587-603, doi:10.1021/cm901452z (2010).
  9. Manthiram, A. Materials Challenges and Opportunities of Lithium Ion Batteries. *Journal of Physical Chemistry Letters* **2**, 176-184, doi:10.1021/jz1015422 (2011).
  10. Marom, R., Amalraj, S. F., Leifer, N., Jacob, D. & Aurbach, D. A review of advanced and practical lithium battery materials. *Journal of Materials Chemistry* **21**, 9938-9954, doi:10.1039/c0jm04225k (2011).
  11. Scrosati, B., Hassoun, J. & Sun, Y.-K. Lithium-ion batteries. A look into the future. *Energy & Environmental Science* **4**, 3287-3295, doi:10.1039/c1ee01388b (2011).
  12. Tarascon, J. M. Key challenges in future Li-battery research. *Philosophical Transactions of the Royal Society a-Mathematical Physical and Engineering Sciences* **368**, 3227-3241, doi:10.1098/rsta.2010.0112 (2010).
  13. Thackeray, M. M., Wolverton, C. & Isaacs, E. D. Electrical energy storage for transportation-approaching the limits of, and going beyond, lithium-ion batteries. *Energy & Environmental Science* **5**, 7854-7863, doi:10.1039/c2ee21892e (2012).
  14. Wagner, F. T., Lakshmanan, B. & Mathias, M. F. Electrochemistry and the Future of the Automobile. *Journal of Physical Chemistry Letters* **1**, 2204-2219, doi:10.1021/jz100553m (2010).
  15. Zhang, Q., Uchaker, E., Candelaria, S. L. & Cao, G. Nanomaterials for energy conversion and storage. *Chemical Society Reviews* **42**, 3127-3171, doi:10.1039/c3cs00009e (2013).
  16. Kim, S. W. & Cho, K. Y. Current Collectors for Flexible Lithium Ion Batteries: A Review of Materials. *Journal of Electrochemical Science and Technology* **6**, 1-6,

- doi:10.5229/jecst.2015.6.1.1 (2015).
17. Kulova, T. L. New electrode materials for lithium-ion batteries (Review). *Russian Journal of Electrochemistry* **49**, 1-25, doi:10.1134/s1023193513010102 (2013).
  18. Li, Y., Song, J. & Yang, J. A review on structure model and energy system design of lithium-ion battery in renewable energy vehicle. *Renewable & Sustainable Energy Reviews* **37**, 627-633, doi:10.1016/j.rser.2014.05.059 (2014).
  19. Behera, S. K. & Raj, R. Extreme-rate capable and highly stable SiCO-TiO<sub>2</sub> hybrids for Li ion battery anodes. *Chemical Communications* **49**, 9657-9659, doi:10.1039/c3cc45311a (2013).

## Chapter 2 - Literature Review

### 2.1 Lithium ion batteries

A rechargeable lithium ion battery is a device that stores and converts chemical energy into electrical energy by the reversible insertion and extraction of Li-ions from the electrodes. A battery technically means a series of one or more interconnected electro- chemical cells each giving a current at a voltage for a time  $\Delta t$  [1]. Like all electro – chemical cells, the secondary lithium ion battery has two electrodes, the cathode (positive) and the anode (negative) which store and shuttle charge, partitioned by a polymeric or ceramic membrane with an electrolyte to transport ions between them. The electrolyte conducts the ions between the anode and the cathode, and the electrons travel in an external circuit when it does work. Oxidation of the Lithium ions take place at the cathode, while reduction takes place at the anode. These reactions are reversible in rechargeable batteries [1-2]. Figure 8 shows a lithium ion secondary cell with the electrodes, the separator and the electrolyte transporting ions.

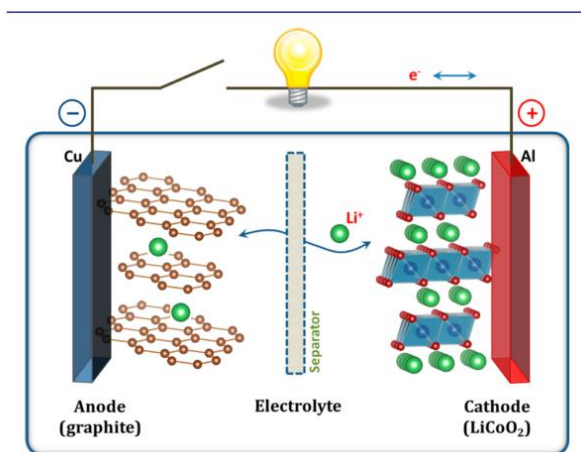


Figure 8 Schematic illustration of the LiCoO<sub>2</sub>/C battery [2]

The capacity of the cell is the charge that can be transferred in a particular unit of time. Capacity is usually measured as specific capacity, i.e. the total charge per unit weight ( $\text{Ahg}^{-1}$ ) or per unit volume ( $\text{AhL}^{-1}$ ) and it depends on the rate of transfer of ions across the electrolyte. The output current  $I$  in a battery can be increased by enlarging the area of the electrodes or connecting cells in parallel [2]. The output power of a battery is dependent of the voltage and current of the battery ( $P = IV$ ). During discharge and charge, an internal battery resistance exists, which lowers down the voltage available across the electrodes from the open circuit voltage when the battery is not working. This can be attributed to the resistance offered by the electrolyte to the ionic current inside the battery. There are irreversible capacity losses in batteries generally due to changes in the electrode volume, (SEI layer formation) or electrode decomposition [1-2].

Compared to other rechargeable batteries, like nickel manganese and lead acid batteries, Li-ion cells exhibit several prominent advantages, namely high gravimetric and volumetric energy density, high working voltage, long service life-time, marginal self-discharge and an enhanced temperature range of operation [1-2]. Figure 9 shows the open circuit diagram of an electrolyte with cathode and anode potentials. The open-circuit voltage of a cell is the difference between the electrochemical potentials  $\mu_A$  and  $\mu_C$  of the anode and cathode:

$$V_{oc} = (\mu_A - \mu_C) / e \dots \dots \dots (1)$$

Figure 10 shows several electrode materials, their working potential against lithium and their specific capacity. The materials close to the bottom are anode materials and those near the top of the graph are high voltage cathode materials. As can be observed, the capacity of the cell is usually limited by the capacity of the cathode material. Lithium phosphates, manganates and compounds of cobalt with metals like nickel and titanium are commonly used cathode materials. Most

commercial batteries have graphite as the anode, but recently Lithium titanate oxide has been commercialized as a high voltage, low capacity anode material for high power application batteries. The schematic in Figure 11 represents the different reaction mechanisms observed in electrode materials for lithium ion batteries. Insertion was the mechanism of lithium

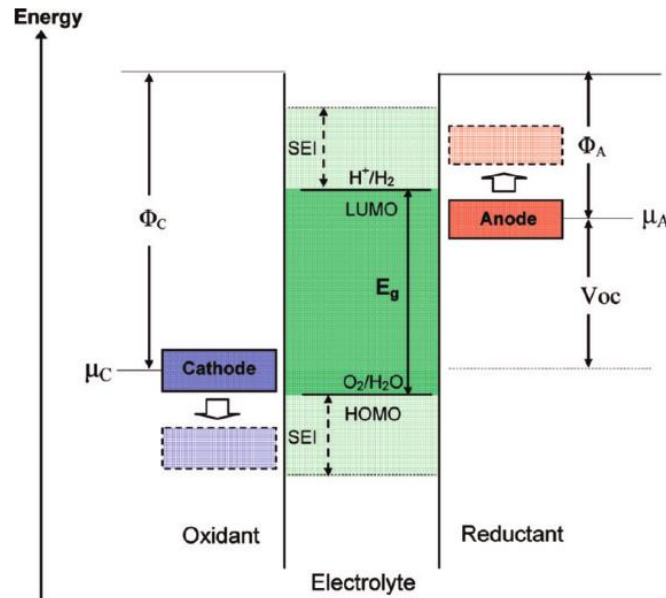


**Figure 9 Open circuit diagram of an electrolyte with cathode and anode potentials [1]**

cycling in the first generation batteries with lithium cobalt oxide cathode and graphite anodes. Though it is the most common mechanism, it suffers with low charge capacity. Alloying reaction of lithium ions with the electrodes provides very large capacities, but this is accompanied by large volume changes and hoop stresses, which limit the cyclability of the electrodes. Conversion electrodes present the new class of materials that are being developed at present. They offer significantly higher capacities than intercalation or insertion electrodes and are structurally more stable than alloying electrodes, even though they suffer from high voltage hysteresis.



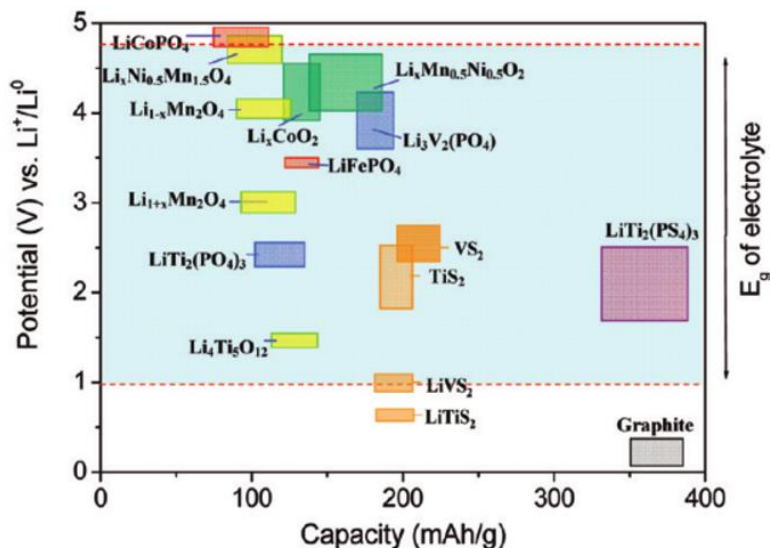


Figure 10 Voltage versus capacity of several electrode materials in  $\text{LiPF}_6$

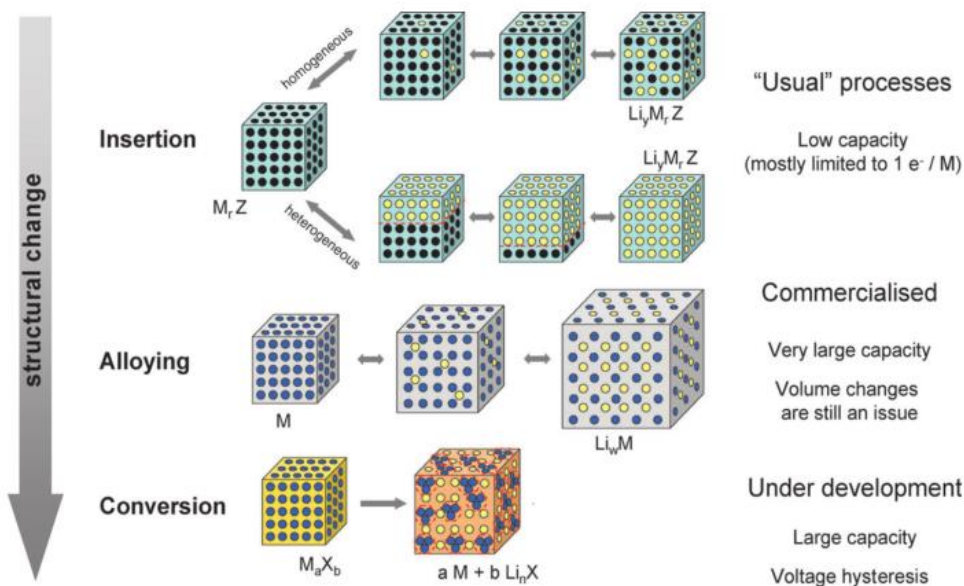
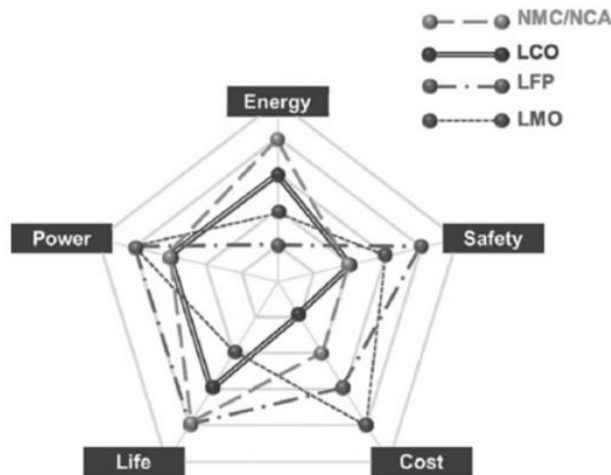


Figure 11 A schematic representation of the different reaction mechanisms observed in electrode materials for lithium batteries [10]

### 2.1.1 Cathode

Cathodes are the positive electrode in batteries. They are generally made up of materials primarily composed of metal calcogenides, transition metal oxides or polyanion compounds. These can further be categorized into layered, spinel, olivine and tavorite [2-7]. Reactions at the electrodes, cathode as well as anode, might take place via three different processes, insertion, alloying or conversion [7-12] and Figure 12 describes the important factors that come into consideration with commercialized cathode materials – eg. layered  $\text{LiMO}_2$  (  $M = \text{Co, Ni}$  or  $\text{Mn}$  with capacities between  $140\text{--}160 \text{ mAh g}^{-1}$ ), spinel  $\text{LiMn}_2\text{O}_4$  with capacities between  $100\text{--}120 \text{ mAh g}^{-1}$  and olivine  $\text{LiFePO}_4$  with capacities between  $140$  and  $160 \text{ mAh g}^{-1}$  [17]. In general, the cell capacity is limited by the capacity of the cathode material.



**Figure 12 Performance criteria of evaluating cathode materials, LCO, NMC,NCA = layered, LMO = spinel, LFP = olivine [17]**

In a typical lithium cell, the cathode is made from lithium cobalt dioxide [13-14] or lithium manganese dioxide [15-20], but other chemistries like Nickel cobalt aluminum (NCA), nickel

manganese cobalt (NMC) are also possible and are used based on properties desired for various applications. Intercalation cathodes are most commonly used in batteries and lithium cobalt dioxide (LiCoO<sub>2</sub>) is the most common material used. Figure 13 shows a comparison of operating voltage and practical capacity of various cathode materials presently used in Li-ion batteries [67]. Since the study of cathodes is beyond the scope of this thesis we will try to explain the reactions at the cathode using a LiCoO<sub>2</sub> intercalation cathode only as the example.

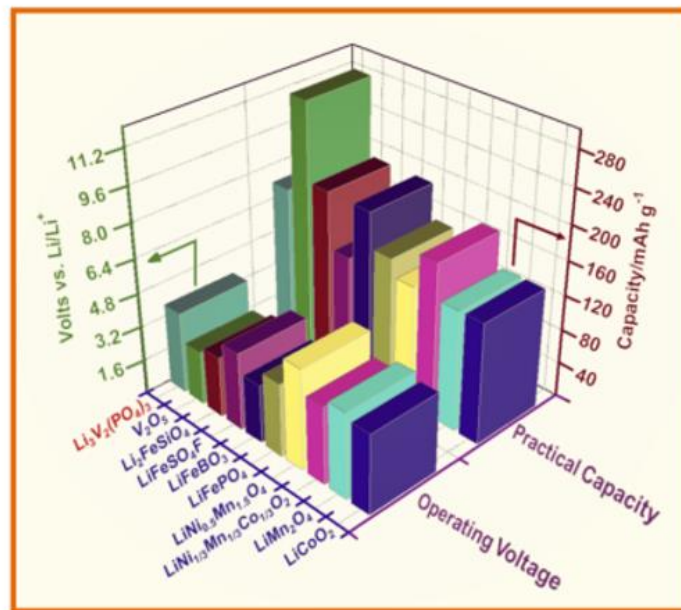


**Figure 13 Comparison of operating voltage and practical capacity of various cathode materials presently used in Li-ion batteries [67]**

When a load is applied and energy is extracted from the battery, electrons flow to the cathode (e.g. Li<sub>1-x</sub>CoO<sub>2</sub>/LiCoO<sub>2</sub>) through the external circuit, while the Li<sup>+</sup> ions get transported to it through the electrolyte because of the potential developed and get reduced there. This reduction reaction can be represented as follows –



When re-charging, an external voltage is applied to the electrodes in the positive direction, reversing the direction of the flow of electrons, Li-ions and the chemical reactions. During the “intercalation” mechanism, there is no actual chemical reaction taking place between the lithium ions and the material of the cathode, but the ions are just physically getting intercalated into the voids in the lattice structure [22-27]. Figure 14 shows the principle of operation by intercalation in a  $\text{LiCoO}_2$ / graphite battery, which was also the first commercial lithium ion battery.

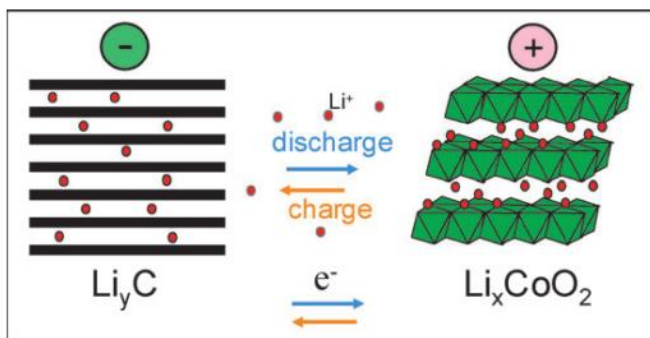


**Figure 14 Principle of operation of the first commercialized lithium-ion batteries [10]**

Using the example of  $\text{LiCoO}_2$  (LCO), the lithium ions occupy the voids between alternative sheets in a cubic close packed array of oxide ions with Co (III). As such, the capacity of the cathode depends on the electrical potential (lithiation) between the ions and the cathode material (vs  $\text{Li/Li}^+$ ). For LCO, this value is 4.2 V and the theoretical capacity of the cathode is limited to around 140 mAh/g. The intercalation of lithium ions into the lattice is a reversible process, but the reversibility of this process decreases at higher voltages (around 4.3V) Thus only 0.5 lithium ions per formula unit can be reinserted which gives a useful capacity of only 150 mAh/g [13-14]

### 2.1.2 Anode

Anodes are the negative electrode in lithium ion batteries, and work on three types of mechanisms just like the cathodes – insertion, alloying and conversion. Graphite, which works on intercalation, is the most widely used material in commercial application as far as anodes are concerned due to various reasons like ease of availability, low cost, thermal and chemical stability, good reversibility, and low delithiation potential vs Li [28-30].

Other anode materials that work on intercalation include carbon based materials like carbon nanotubes and graphene and non-carbon based materials like titanium dioxide (TiO<sub>2</sub>), lithium titanate oxide (Li<sub>4</sub>Ti<sub>5</sub>O<sub>12</sub>/LTO), etc. Figure 15 shows lithium intercalation in the graphite and LTO intercalation anodes.

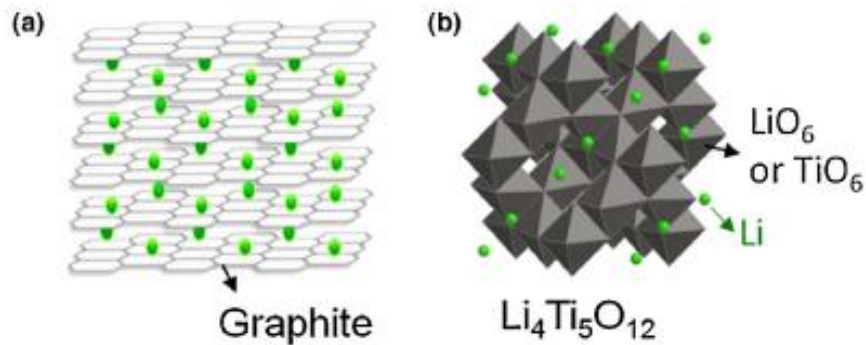


**Figure 15 Graphite and LTO intercalation anodes**

For graphite, the highest stoichiometry that can form at room temperature due to intercalation is LiC<sub>6</sub>, and this provides a theoretical capacity of 372 mAhg<sup>-1</sup> [31-35]. The intercalation reaction that takes place during charging is as follows –



As far as alloying materials are concerned, silicon has proven to be the most promising of the materials researched so far. The lithiation and delithiation mechanism in alloying materials is different from insertion in the sense that the elements electrochemically alloy and form compound phases with Li instead of just providing physical voids in the host lattice for lithium ions to occupy. There are many other elements like tin (Sn), germanium (Ge), aluminum (Al), bismuth (Bi) and tin dioxide ( $\text{SnO}_2$ ) that have been shown to be useful as alloying anodes as well [5, 10, 35]. Figure 16 statistically compares the volumetric and gravimetric specific capacities of various alloying anode materials.

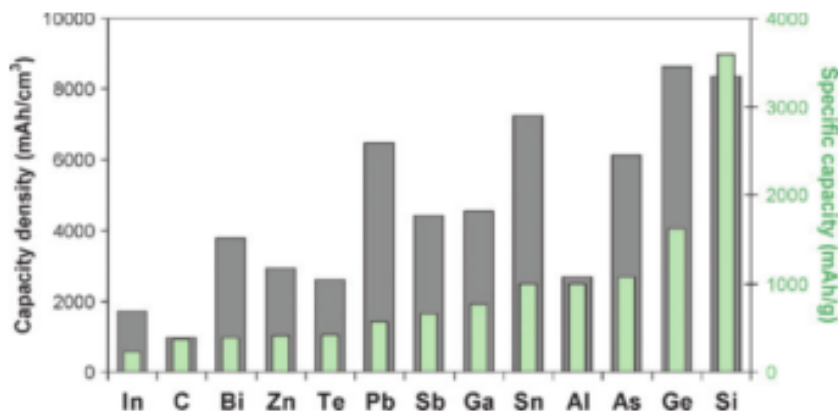


**Figure 16 Specific capacities and capacity densities for selected alloying reactions [10]**

As such, the delithiation potential in these materials is higher compared to insertion materials due to the higher magnitude of Gibbs energy involved. Figure 17 shows lithiation in silicon by alloying. Silicon is found to be most promising because of its relatively low average delithiation potential, ease of availability, and chemical stability and can provide specific capacities greater than 2000 mAh/g [37, 39]. However, cyclability, capacity loss and high cell impedance due to large volume changes and its effect on the SEI layer, limit its practical use. Most

other alloying materials suffer from problems like brittleness, high delithiation potentials and even toxicity in some cases [36-41].

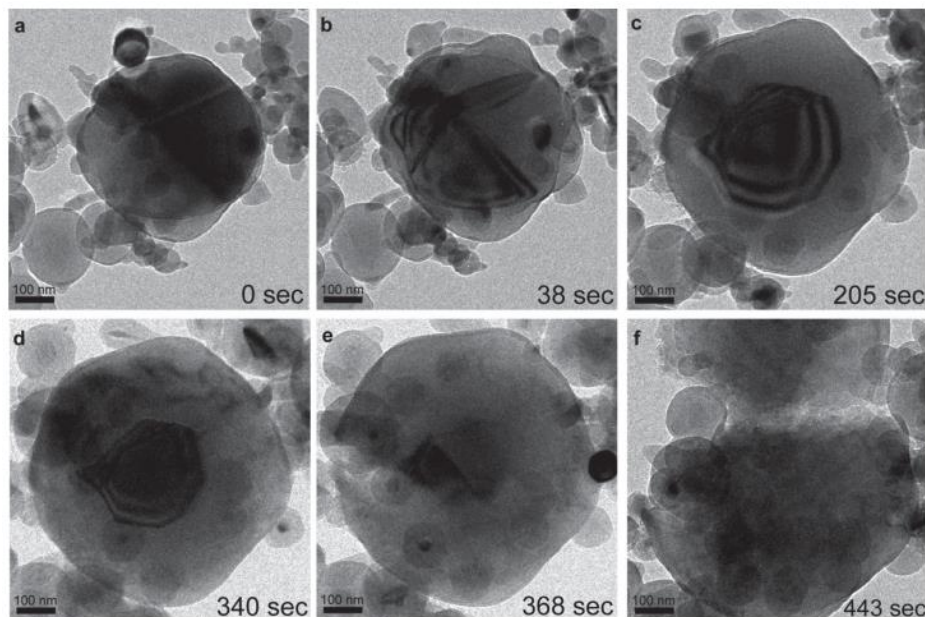
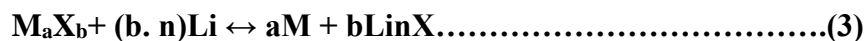


**Figure 17 Alloying reaction in a Silicon anode [39]**

Recently, there is growing interest in electrochemical reaction of lithium transition metal dichalcogenides because of their unique conversion reaction mechanism which is as follows:



where M is transition metal, X anion and n is formal oxidation state of X. Conversion reactions were studied earlier as well, but were abandoned because of the simplicity of intercalation mechanisms. However, when it was realized that the capacity through these reactions can be as much as three times that of graphite, there was renewed interest in them [68]. During lithiation metal non domains are formed as shown in Figure 18. These domains have high surface

reactivity and can decompose lithium binary compounds ( $\text{Li}_2\text{X}$ ) in which they are embedded when a reverse polarization is applied. The success of conversion reaction mechanism lies with nano-domain metallic particles which is maintained even after many charge/discharge cycles. The actual potential at which these reactions occur depends on the transition metal and the anionic species. This gives a level of variability to the requirement of specific applications [68].

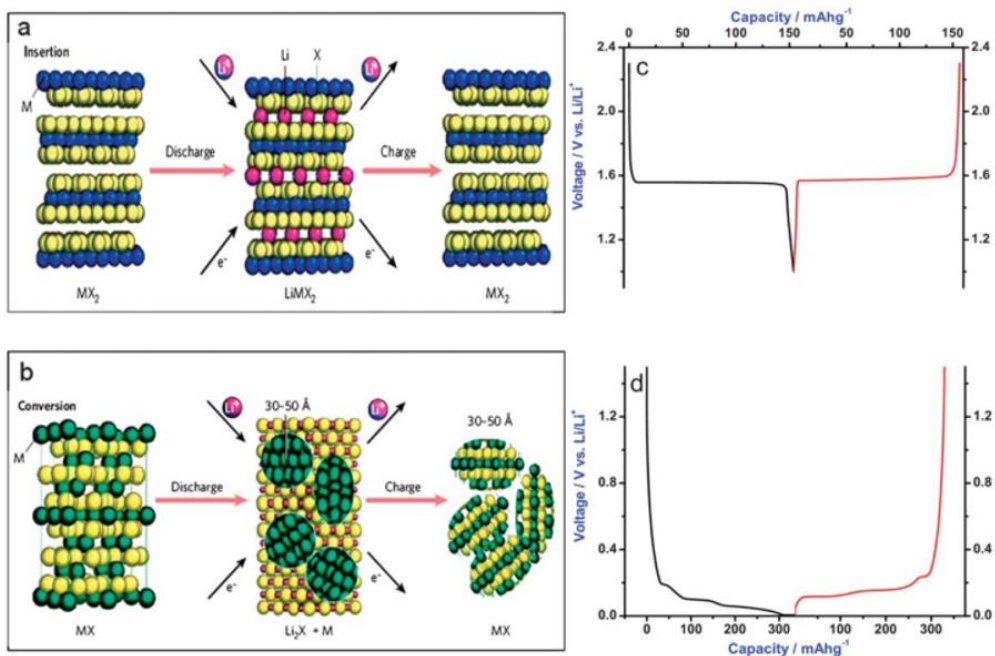


**Figure 18 Intercalation and conversion reaction mechanisms [68]**

### 2.1.3 Electrolyte

Conventional lithium-ion battery electrolytes consist of  $\text{LiPF}_6$  dissolved in a mixture of organic solvents. These solutions offer very high ionic conductivities and are compatible with the battery voltage operation window. They are usually based on carbonate solvents, which are aprotic, polar and have a high dielectric constant, which enables them to solvate lithium salts to high concentrations [10]. Commercial mixtures differ depending on the manufacturer, but generally



contain two to four solvents, one of them always being ethylene carbonate (EC), which has a high dielectric constant [10].

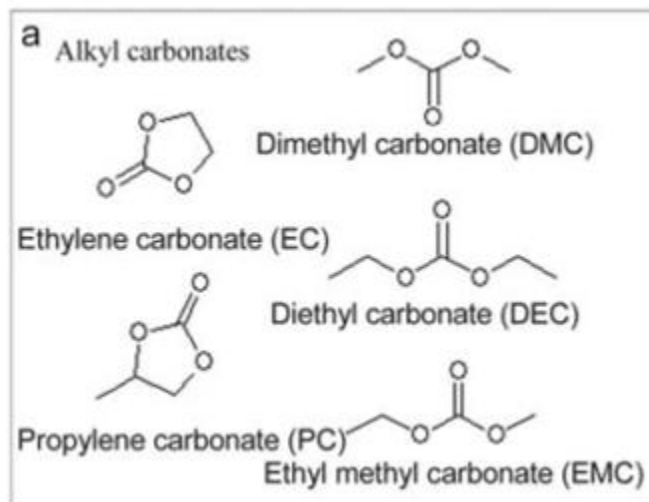


**Figure 19 Common electrolyte solvents [68]**

## 2.3 Polymer derived ceramics

### 2.3.1 Introduction

Polymer derived ceramics (PDCs) are compounds which are prepared by a controlled thermal degradation of inorganic liquid polymer precursors. PDCs are generally classified as binary ( $\text{SiC}$ ,  $\text{Si}_3\text{N}_4$ ,  $\text{BN}$ ,  $\text{BC}$  and  $\text{B}_2\text{O}_3$ ), tertiary ( $\text{SiCN}$ ,  $\text{SiBC}$ ,  $\text{SiCO}$  and  $\text{BCN}$ ) or quaternary ( $\text{SiBCN}$ ,  $\text{SiBCO}$ ,  $\text{SiAlCO}$ ,  $\text{SiCNO}$ ) based on the number of constituent elements in the synthesized final ceramic and offer remarkable engineering properties such as very high thermal and chemical stability, photoluminescence and some of them even exhibit semiconducting behavior at high temperatures [42, 44, 46]. As shown in figure 20, R1 and R2 can be organic functional groups and -X- can be -O-, -C- or -N-. As an example, a variation of the group (X) in the general structure can give result to various classes of precursors such as polyorganosilanes ( $\text{X}=\text{Si}$ ), polyorganocarbo-silanes ( $\text{X}=\text{CH}_2$ ),

polyorganosilazanes (X=NH), polyorganosilylcarbodiimides (X= [ N=C=N]) [55]. Figure 21 shows in brief, the structure and conversion process to obtain the most common SiOC and SiCN ceramics.

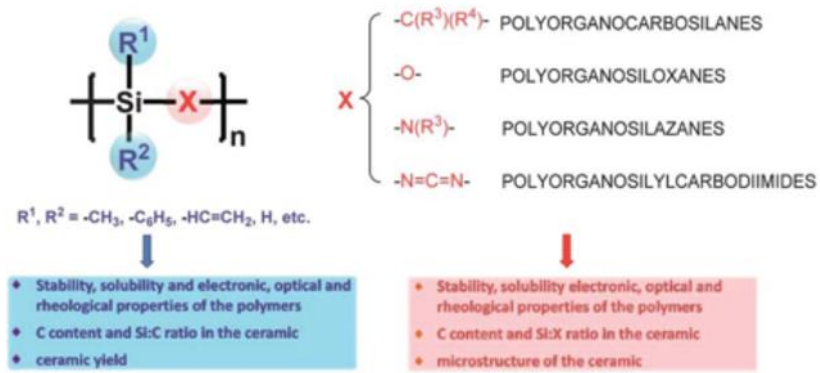


**Figure 20 General chemical formula for PDCs [55]**

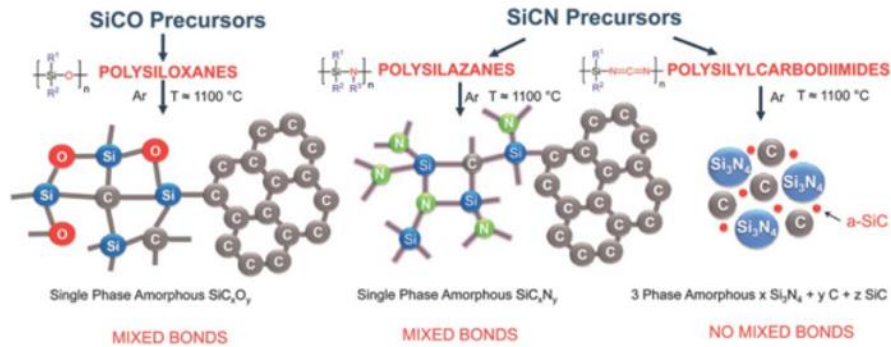


**Figure 21 Showing SiOC and SiCN precursors and ceramics [55]**

The process of forming a solid ceramic from a liquid polymer is actually a two-step process. In the first step the liquid polymeric precursor is shaped and/or cross-linked by heating it to ~400 °C in an inert medium. Cross-linking results in increased bonding between the elements of the precursor leading to highly interconnected backbone (Si-C, Si-O, etc.), reducing the volatility of the crosslinked product and increasing the ceramic yield [49-51]. There are numerous ways to

synthesize the ceramic, and the path taken depends on the final application desired. Figure 22 gives a comprehensive description of the polymer to ceramic transformation and the different pathways involved.

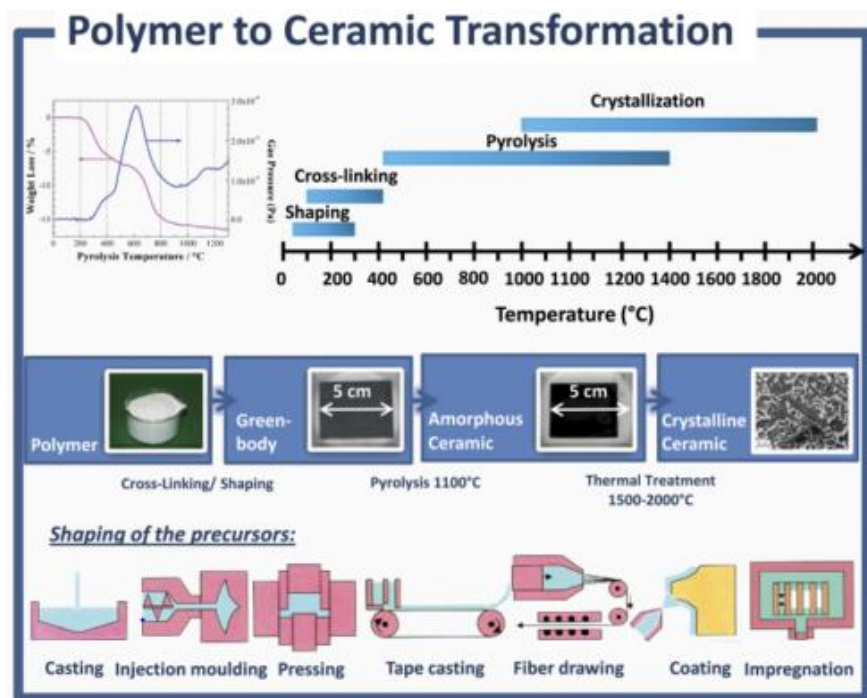


**Figure 22 Polymer to ceramic transformation [52]**

Cross-linking silyl functional groups are intentionally added to the polymer precursor for effective cross-linking. Followed by crosslinking, pyrolysis is carried out at 800- 1400 °C under inert conditions. During pyrolysis, there is weight loss observed in the material. This weight loss is mainly attributed to the release of gases which are formed due to the various reactions at different temperature ranges. Oligomers evaporate at lower temperatures due to hydrosilylation and ammonia gas is released due to transamination. At higher temperature the evolution of hydrocarbons (e.g. CH<sub>4</sub>, C<sub>2</sub>H<sub>6</sub> etc.) and hydrogen results in further weight loss. Due to the thermal induced decomposition and the release of hydrocarbons and other volatile compounds, the cross-linked polymer consolidates to amorphous ceramic. More hydrogen is retained at lower processing

temperatures (~800 °C). Annealing (beyond 1400°C) results in nucleation and growth of nano-sized crystalline phases in the ceramic. Meanwhile, depending on the polymer chemical structure and composition, precipitation of free  $sp^2$  bonded carbon occurs during the polymer to ceramic conversion between 600 - 800°C [52-58]. Figure 23 shows the free carbon network in a silicon carbo nitrile PDC. Figure 24 shows the EF - TEM image of SiOC. The free carbon in these polymer derived ceramics is the source of many of their electro chemical properties.

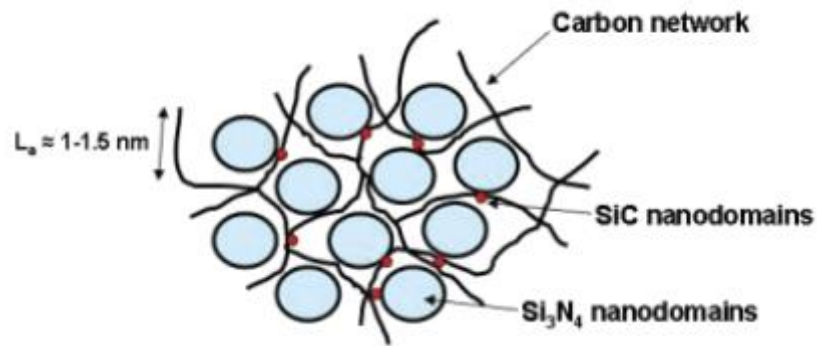


**Figure 23 Microstructural model for SiCN ceramic [52]**

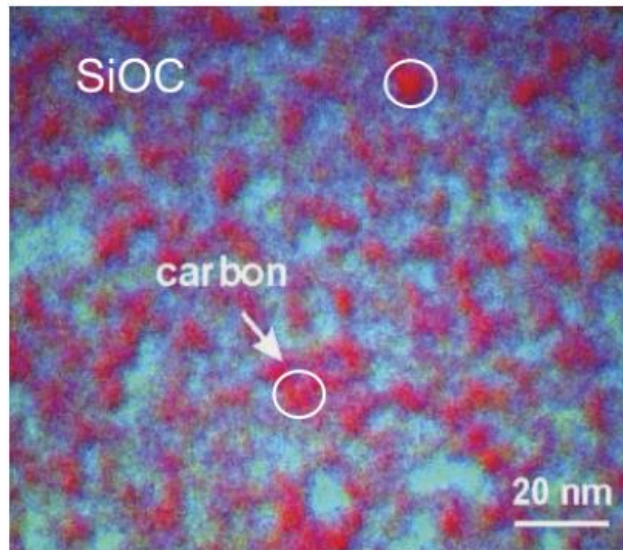


**Figure 24 EF-TEM image of a carbon-rich SiCO ceramic showing “free” carbon phase [52]**

Most of the properties of PDCs are tunable and Figure 25 describes this diagrammatically. The reason for these remarkable properties has been identified as the temperature dependent microstructure of PDCs, which consists of  $-sp^2$  bonded carbon network along with nanodomains of silicon mixed bond tetrahedra (Si/B/C/N/O bonds) [44]. PDCs differ from other conventional ceramics in several ways. Since they are derived from a liquid polymer, process flexibility allows the altering of the processing conditions and composition of the initial polymeric precursor. Unique features to attain near net shape of the desired structure, controlled molecular structure of the final ceramic based on precursor chemistry, ease of synthesizing a composite, processing temperatures and elemental doping the final ceramic with desired electrical, thermal, mechanical and electrochemical property can be synthesized [45-47]

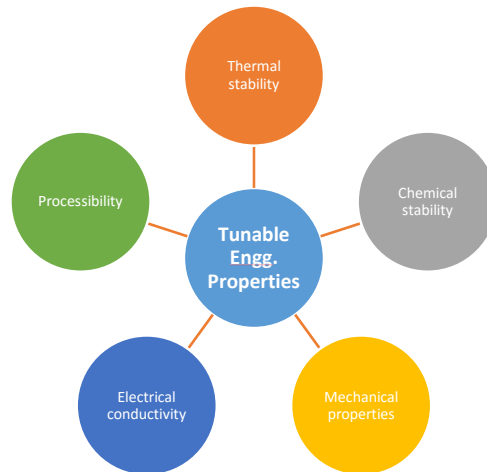


**Figure 25 Tunable engineering properties for PDCs- [44]**

Figure 26 describes the temperature dependence of electrical resistance of SiCO and SiBCO ceramics annealed at 1300°C. As can be observed, the electrical resistance depends on the annealing time and the presence of boron in the precursor. Boron free ceramics annealed for the longest time have the least electrical resistance and boron containing ceramics annealed for the

shortest time have the highest electrical resistance [45]. This is just one example of how the final properties of the ceramic can be tailored depending on the application and requirement.

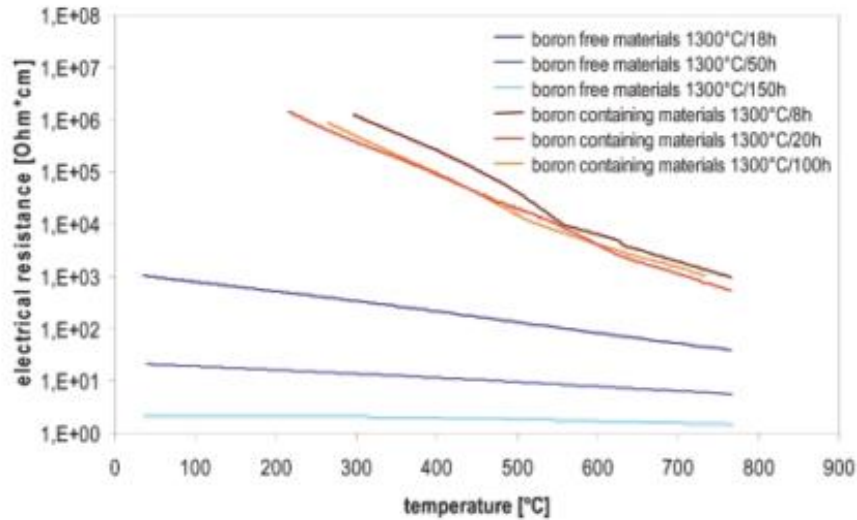


**Figure 26 Temperature dependence of electrical resistance of SiCO and SiBCO ceramics annealed at 1300°C for different times [45]**

As PDCs can be shaped using a wide variety of processing methods and there is considerable amount of control over their physical, chemical and functional properties they have found application in several key fields such as information technology, transport, defense, energy as well as environmental systems, biomedical components and micro- or nanoelectromechanical systems (MEMS/NEMS). Most common applications of PDCs are their use as fibers, ceramic – matrix composites, highly porous components, micro components and as coatings. Figure 27 describes some selected applications.

The discussion in this work is limited to polysiloxane precursors, which results in the formation of silicon oxy carbide (SiOC) PDCs and their application in Lithium – ion batteries.

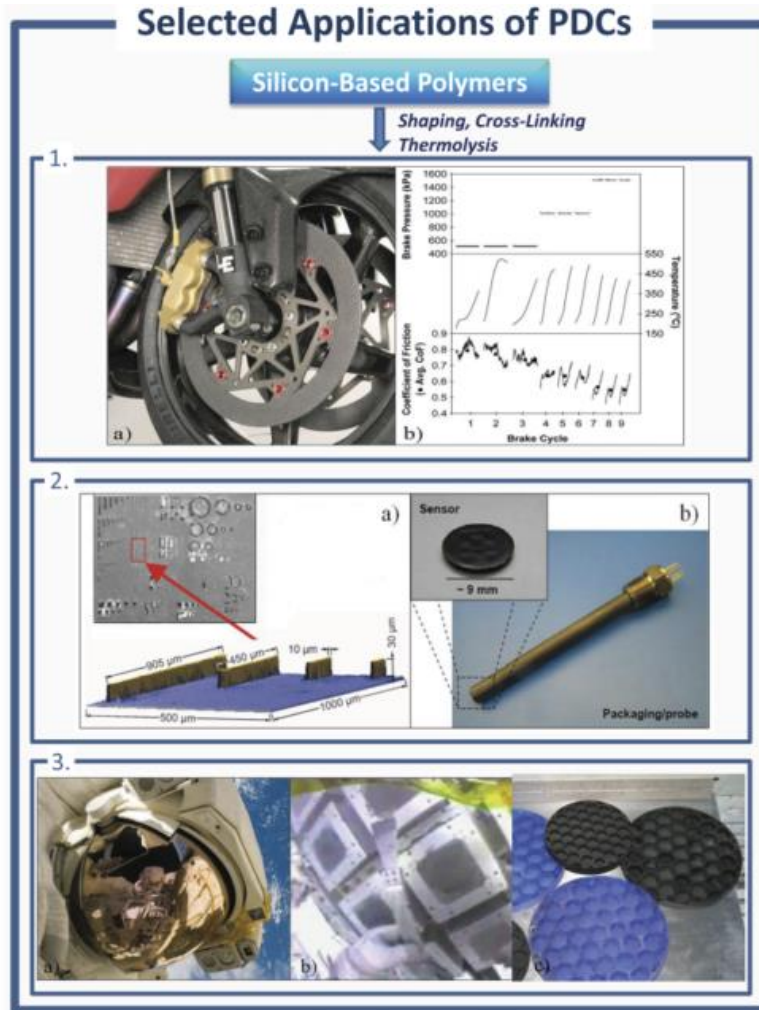


**Figure 27 Selected applications of PDCs [52]**

### 2.3.2 Silicon oxy-carbide

Silicon oxycarbide is a compound of silicon, carbon and oxygen, in which silicon is bonded to carbon and oxygen in the form of tetrahedral structural units with mixed bonds. It is derived from 1,3,5,7 – tetra vinyl – 1,3,5,7 - tetramethylcyclotetrasiloxane (TTCS) polymer, the structure of which is shown in Figure 28. The final ceramic material can be quite heterogeneous with regions of high concentration areas of Si-O-C network, free carbon and SiO<sub>2</sub>-enriched regions [52, 60].

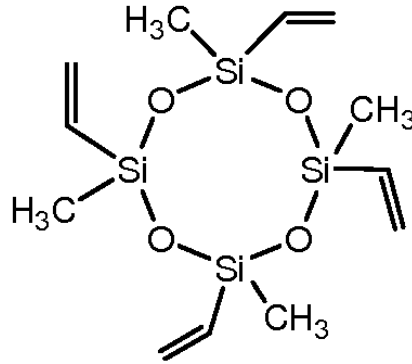


**Figure 28 TTCS chemical structure**

When the term “carbon-rich” is used, it means the ceramic contains carbon more than 20% by weight. Figure 29 shows the inter-domain boundaries containing graphene layers with mixed Si-C-O bonds. Figure 30 shows a scanning electron microscope (SEM) image of the SiOC ceramic magnified up to 20  $\mu\text{m}$ . The image shows that the material is glassy in nature, hence the size of the particles is crucial in the final ceramic.

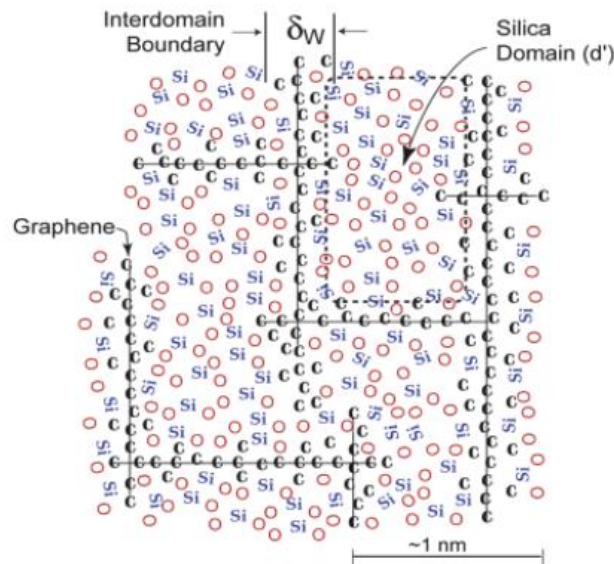


**Figure 29 Schematic showing inter-domain boundaries containing graphene layers with mixed Si-C-O bonds [52]**





**Figure 30 SEM image of the Si-O-C composite under a hydrogen atmosphere [57]**

Depending on the amount of segregated carbon, either carbon nano-domains exist, which means lower amount of free carbon or a carbon percolation network exists, which means a higher amount of free carbon. This can be demonstrated and measured by electrical conductivity measurements and TEM analysis. Carbon rich SiOC has more enhanced temperature resistance and high temperature crystallization integrity [59-65]

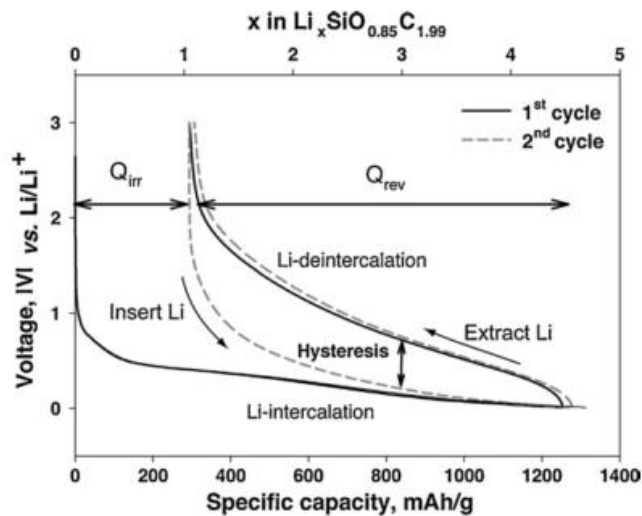


**Figure 31 The insertion and extraction of lithium into polymer-derived SiCO is hysteretic [66]**

Figure 31 shows the extraction and insertion of lithium ions into polymer derived ceramic showing hysteresis losses for the first two cycles [66]. Silicon oxy carbide of various stoichiometry has been studied as a potential anode material for Li – ion batteries. In general, it exhibits high capacities (upto  $1000 \text{ mAhg}^{-1}$ ), but this capacity is known to degrade very quickly, within 50 cycles as shown in figure 32 [44]. As the electrochemical properties of polymer derived silicon oxy carbide depends on the precursors and the starting materials, this research is focused on enhancing the cycling capacity of SiOC by forming a hybrid with titanium dioxide as was explained in the previous chapter.

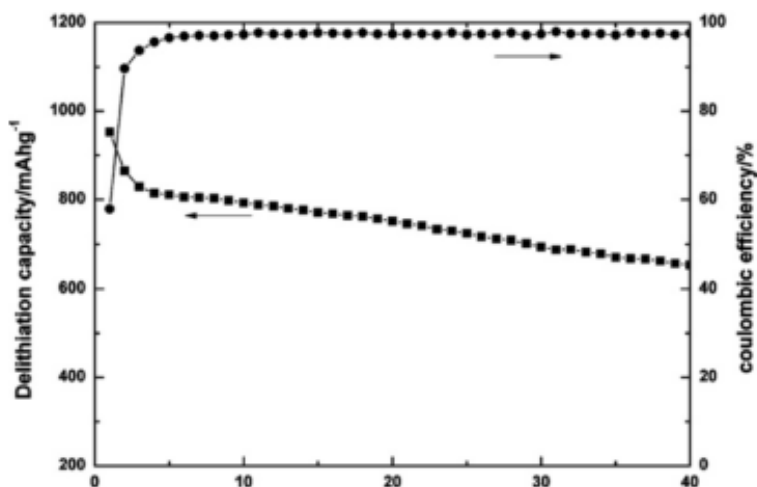


Figure 32 Showing capacity degradation in silicon oxy carbide [44]

## References

- 1 Goodenough, J. B. & Kim, Y. Challenges for Rechargeable Li Batteries. *Chemistry of Materials* **22**, 587-603, doi:10.1021/cm901452z (2010).
- 2 Goodenough, J. B. & Park, K.-S. The Li-Ion Rechargeable Battery: A Perspective.

- Journal of the American Chemical Society* **135**, 1167-1176, doi:10.1021/ja3091438 (2013).
- 3 Yi, T., Yue, C., Zhu, Y., Zhu, R. & Hu, X. A Review of Research on Cathode Materials for Power Lithium Ion Batteries. *Rare Metal Materials and Engineering* **38**, 1687-1692 (2009).
- 4 Chen, Z., Zhang, C., Zhang, Z. & Li, J. Correlation of intercalation potential with d-electron configurations for cathode compounds of lithium-ion batteries. *Physical Chemistry Chemical Physics* **16**, 13255-13261, doi:10.1039/c4cp00855c (2014).
- 5 Rommel, S. M., Schall, N., Bruenig, C. & Wehrich, R. Challenges in the synthesis of high voltage electrode materials for lithium-ion batteries: a review on LiNiPO<sub>4</sub>. *Monatshefte Fur Chemie* **145**, 385-404, doi:10.1007/s00706-013-1134-0 (2014).
- 6 Rui, X., Yan, Q., Skyllas-Kazacos, M. & Lim, T. M. Li<sub>3</sub>V<sub>2</sub>(PO<sub>4</sub>)<sub>3</sub> cathode materials for lithium-ion batteries: A review. *Journal of Power Sources* **258**, 19-38, doi:10.1016/j.jpowsour.2014.01.126 (2014).
- 7 Verrelli, R., Scrosati, B., Sun, Y.-K. & Hassoun, J. Stable, High Voltage Li<sub>0.85</sub>Ni<sub>0.46</sub>Cu<sub>0.1</sub>Mn<sub>1.49</sub>O<sub>4</sub> Spinel Cathode in a Lithium-Ion Battery Using a Conversion-Type CuO Anode. *Acs Applied Materials & Interfaces* **6**, 5206-5211, doi:10.1021/am500499a (2014).
- 8 Watanabe, T. *et al.* Characterization of vanadium oxide sol as a starting material for high rate intercalation cathodes. *Solid State Ionics* **151**, 313-320, doi:10.1016/s0167-2738(02)00729-4 (2002).
- 9 Wu, H., Liu, Q. & Guo, S. Composites of Graphene and LiFePO<sub>4</sub> as Cathode Materials for Lithium-Ion Battery: A Mini-review. *Nano-Micro Letters* **6**, 316-326,

- doi:10.1007/s40820-014-0004-6 (2014).
- 10 Rosa Palacin, M. Recent advances in rechargeable battery materials: a chemist's perspective. *Chemical Society Reviews* **38**, 2565-2575, doi:10.1039/b820555h (2009).
- 11 Wu, Z.-J. *et al.* A novel conversion of converter sludge into amorphous multi-doped FePO<sub>4</sub> cathode material for lithium ion batteries. *Scripta Materialia* **67**, 221-224, doi:10.1016/j.scriptamat.2012.04.027 (2012).
- 12 Li, T., Chen, Z. X., Ai, X. R., Cao, Y. L. & Yang, H. X. LiF/Fe nanocomposite as a lithium-rich and high capacity conversion cathode material for Li-ion batteries. *Journal of Power Sources* **217**, 54-58, doi:10.1016/j.jpowsour.2012.05.111 (2012).
- 13 Jang, Y. I. *et al.* LiAl<sub>y</sub>Co<sub>1-y</sub>O<sub>2</sub> ( $R\bar{3}m$ ) intercalation cathode for rechargeable lithium batteries. *Journal of the Electrochemical Society* **146**, 862-868, doi:10.1149/1.1391693 (1999).
- 14 Jang, Y. I., Neudecker, B. J. & Dudney, N. J. Lithium diffusion in Li<sub>x</sub>CoO<sub>2</sub> ( $0.45 < x < 0.7$ ) intercalation cathodes. *Electrochemical and Solid State Letters* **4**, A74-A77, doi:10.1149/1.1368717 (2001).
- 15 Zhao, X. *et al.* Structure Design and Performance of LiNi<sub>x</sub>Co<sub>y</sub>Mn<sub>1-x-y</sub>O<sub>2</sub> Cathode Materials for Lithium-ion Batteries: A Review. *Journal of the Chinese Chemical Society* **61**, 1071-1083, doi:10.1002/jccs.201400107 (2014).
- 16 Ren, X.-D., Liu, J.-J. & Zhang, W.-Q. Strain effect on the intercalation potential of the layered Mn-contained lithium ion batteries cathode materials: a first principles method. *Acta Physica Sinica* **61**, doi:10.7498/aps.61.183101 (2012).
- 17 Dou, S. Review and prospect of layered lithium nickel manganese oxide as cathode materials for Li-ion batteries. *Journal of Solid State Electrochemistry* **17**, 911-926,

- doi:10.1007/s10008-012-1977-z (2013).
- 18 Robertson, A. D., Lu, S. H., Averill, W. F. & Howard, W. F. M<sup>3+</sup>-modified LiMn<sub>2</sub>O<sub>4</sub> spinel intercalation cathodes .1. Admetal effects on morphology and electrochemical performance. *Journal of the Electrochemical Society* **144**, 3500-3505, doi:10.1149/1.1838040 (1997).
- 19 Robertson, A. D., Lu, S. H. & Howard, W. F. M<sup>3+</sup>-modified LiMn<sub>2</sub>O<sub>4</sub> spinel intercalation cathodes .2. Electrochemical stabilization by Cr<sup>3+</sup>. *Journal of the Electrochemical Society* **144**, 3505-3512, doi:10.1149/1.1838041 (1997).
- 20 Yi, T.-F., Hao, C.-L., Yue, C.-B., Zhu, R.-S. & Shu, J. A literature review and test: Structure and physicochemical properties of spinel LiMn<sub>2</sub>O<sub>4</sub> synthesized by different temperatures for lithium ion battery. *Synthetic Metals* **159**, 1255-1260, doi:10.1016/j.synthmet.2009.02.026 (2009).
- 21 Cho, J., Kim, Y. J., Kim, T. J. & Park, B. Zero-strain intercalation cathode for rechargeable Li-ion cell. *Angewandte Chemie-International Edition* **40**, 3367-+, doi:10.1002/1521-3773(20010917)40:18<3367::aid-anie3367>3.0.co;2-a (2001).
- 22 Thissen, A. *et al.* Experimental routes to in situ characterization of the electronic structure and chemical composition of cathode materials for lithium ion batteries during lithium intercalation and deintercalation using photoelectron spectroscopy and related techniques. *Ionics* **15**, 393-403, doi:10.1007/s11581-009-0339-z (2009).
- 23 Viswanathan, V. V. *et al.* Effect of entropy change of lithium intercalation in cathodes and anodes on Li-ion battery thermal management. *Journal of Power Sources* **195**, 3720-3729, doi:10.1016/j.jpowsour.2009.11.103 (2010).
- 24 Zhang, X., Sastry, A. M. & Shyy, W. Intercalation-induced stress and heat generation

- within single lithium-ion battery cathode particles. *Journal of the Electrochemical Society* **155**, A542-A552, doi:10.1149/1.2926617 (2008).
- 25 Zhao, Y. *et al.* Stable Alkali Metal Ion Intercalation Compounds as Optimized Metal Oxide Nanowire Cathodes for Lithium Batteries. *Nano Letters* **15**, 2180-2185, doi:10.1021/acs.nanolett.5b00284 (2015).
- 26 Zheng, J. P., Crain, D. J. & Roy, D. Kinetic aspects of Li intercalation in mechano-chemically processed cathode materials for lithium ion batteries: Electrochemical characterization of ball-milled LiMn<sub>2</sub>O<sub>4</sub>. *Solid State Ionics* **196**, 48-58, doi:10.1016/j.ssi.2011.06.004 (2011).
- 27 Armand, M. & Touzain, P. GRAPHITE INTERCALATION COMPOUNDS AS CATHODE MATERIALS. *Materials Science and Engineering* **31**, 319-329, doi:10.1016/0025-5416(77)90052-0 (1977).
- 28 He, L. *et al.* Electrochemical characteristics and intercalation mechanism of ZnS/C composite as anode active material for lithium-ion batteries. *Electrochimica Acta* **56**, 1213-1218, doi:10.1016/j.electacta.2010.11.014 (2011).
- 29 Kalnaus, S., Rhodes, K. & Daniel, C. A study of lithium ion intercalation induced fracture of silicon particles used as anode material in Li-ion battery. *Journal of Power Sources* **196**, 8116-8124, doi:10.1016/j.jpowsour.2011.05.049 (2011).
- 30 Kim, Y., Hwang, H., Yoon, C. S., Kim, M. G. & Cho, J. Reversible lithium intercalation in teardrop-shaped ultrafine SnP<sub>0.94</sub> particles: An anode material for lithium-ion batteries. *Advanced Materials* **19**, 92-+, doi:10.1002/adma.200600644 (2007).
- 31 Rui, X. H., Yesibolati, N. & Chen, C. H. Li<sub>3</sub>V<sub>2</sub>(PO<sub>4</sub>)<sub>3</sub>/C composite as an

- intercalation-type anode material for lithium-ion batteries. *Journal of Power Sources* **196**, 2279-2282, doi:10.1016/j.jpowsour.2010.09.024 (2011).
- 32 Shao, L. *et al.* Electrochemical Characteristics and Intercalation Mechanism of Manganese Carbonate as Anode Material for Lithium-Ion Batteries. *International Journal of Electrochemical Science* **8**, 1170-1180 (2013).
- 33 Wang, F. *et al.* Sandwich-like Cr<sub>2</sub>O<sub>3</sub>-graphite intercalation composites as high-stability anode materials for lithium-ion batteries. *Journal of Materials Chemistry A* **3**, 1703-1708, doi:10.1039/c4ta05072j (2015).
- 34 Wang, F. *et al.* Graphite Intercalation Compounds (GICs): A New Type of Promising Anode Material for Lithium-Ion Batteries. *Advanced Energy Materials* **4**, doi:10.1002/aenm.201300600 (2014).
- 35 Besenhard, J. O., Yang, J. & Winter, M. Will advanced lithium-alloy anodes have a chance in lithium-ion batteries? *Journal of Power Sources* **68**, 87-90, doi:10.1016/s0378-7753(96)02547-5 (1997).
- 36 Ferguson, P. P., Todd, A. D. W. & Dahn, J. R. Comparison of mechanically alloyed and sputtered tin-cobalt-carbon as an anode material for lithium-ion batteries. *Electrochemistry Communications* **10**, 25-31, doi:10.1016/j.elecom.2007.10.025 (2008).
- 37 Ge, M., Fang, X., Rong, J. & Zhou, C. Review of porous silicon preparation and its application for lithium-ion battery anodes. *Nanotechnology* **24**, doi:10.1088/0957-4484/24/42/422001 (2013).
- 38 Li, H., Shi, L. H., Wang, Q., Chen, L. Q. & Huang, X. J. Nano-alloy anode for lithium ion batteries. *Solid State Ionics* **148**, 247-258, doi:10.1016/s0167-2738(02)00061-9

- (2002).
- 39 McDowell, M. T., Lee, S. W., Nix, W. D. & Cui, Y. 25th Anniversary Article: Understanding the Lithiation of Silicon and Other Alloying Anodes for Lithium-Ion Batteries. *Advanced Materials* **25**, 4966-4984, doi:10.1002/adma.201301795 (2013).
- 40 Obrovac, M. N., Christensen, L., Le, D. B. & Dahnb, J. R. Alloy design for lithium-ion battery anodes. *Journal of the Electrochemical Society* **154**, A849-A855, doi:10.1149/1.2752985 (2007).
- 41 West, N., Ozoemena, K. I., Ikpo, C. O., Baker, P. G. L. & Iwuoha, E. I. Transition metal alloy-modulated lithium manganese oxide nanosystem for energy storage in lithium-ion battery cathodes. *Electrochimica Acta* **101**, 86-92, doi:10.1016/j.electacta.2012.11.085 (2013).
- 42 Duong, B. *et al.* Printed Sub-100 nm Polymer-Derived Ceramic Structures. *Acs Applied Materials & Interfaces* **5**, 3894-3899, doi:10.1021/am400587z (2013).
- 43 Erdem, E. *et al.* Defect structure in lithium-doped polymer-derived SiCN ceramics characterized by Raman and electron paramagnetic resonance spectroscopy. *Physical Chemistry Chemical Physics* **11**, 5628-5633, doi:10.1039/b822457a (2009).
- 44 R. Bhandavat, Z. Pei, G. Singh, Polymer-derived ceramics as anode material for rechargeable Li-ion batteries: a review. *Nanomaterials and Energy* **1**, 324-327 (2012)
- 45 Riedel, R., Mera, G., Hauser, R. & Klönczyski, A. Silicon-based polymer-derived ceramics: Synthesis properties and applications - A review. *Journal of the Ceramic Society of Japan* **114**, 425-444, doi:10.2109/jcersj.114.425 (2006).
- 46 Schulz, M. Polymer derived ceramics in MEMS/NEMS - a review on production processes and application. *Advances in Applied Ceramics* **108**, 454-460,



- doi:10.1179/174367609x422171 (2009).
- 47 Colombo, P., Hellmann, J. R. & Shelleman, D. L. Mechanical properties of silicon oxycarbide ceramic foams. *Journal of the American Ceramic Society* **84**, 2245-2251
- 48 Corriu, R. J. P., Leclercq, D., Mutin, P. H. & Vioux, A. Preparation and structure of silicon oxycarbide glasses derived from polysiloxane precursors. *Journal of Sol-Gel*
- 49 Kamiya, K. *et al.* Preparation of silicon oxycarbide glass fibers by sol-gel method - Effect of starting sol composition on tensile strength of fibers. *Journal of Sol-Gel Science and Technology* **14**, 95-102, doi:10.1023/a:1008784032647 (1999).
- 50 Kim, Y. W., Kim, S. H. & Park, C. B. Processing of closed-cell silicon oxycarbide foams from a preceramic polymer. *Journal of Materials Science* **39**, 5647-5652, doi:10.1023/b:jmsc.0000040071.55240.85 (2004).
- 51 Kroll, P. Modelling and simulation of amorphous silicon oxycarbide. *Journal of Materials Chemistry* **13**, 1657-1668, doi:10.1039/b301389h (2003).
- 52 Colombo, P., Mera, G., Riedel, R. & Soraru, G. D. Polymer-Derived Ceramics: 40 Years of Research and Innovation in Advanced Ceramics. *Journal of the American Ceramic Society* **93**, 1805-1837, doi:10.1111/j.1551-2916.2010.03876.x (2010).
- 53 Kroll, P. Modeling the 'free carbon' phase in amorphous silicon oxycarbide. *Journal of Non-Crystalline Solids* **351**, 1121-1126, doi:10.1016/j.jnoncrysol.2005.01.010 (2005).
- 54 Liu, Q., Shi, W., Babonneau, F. & Interrante, L. V. Synthesis of polycarbosilane/siloxane hybrid polymers and their pyrolytic conversion to silicon oxycarbide ceramics. *Chemistry of Materials* **9**, 2434-2441, doi:10.1021/cm970316e
- 55 Mera, G., Navrotsky, A., Sen, S., Kleebe, H.-J. & Riedel, R. Polymer-derived SiCN and SiOC ceramics - structure and energetics at the nanoscale. *Journal of Materials*

- Chemistry A* **1**, 3826-3836, doi:10.1039/c2ta00727d (2013).
- 56 Mera, G., Tamayo, A., Nguyen, H., Sen, S. & Riedel, R. Nanodomain Structure of Carbon-Rich Silicon Carbonitride Polymer-Derived Ceramics. *Journal of the American Ceramic Society* **93**, 1169-1175, doi:10.1111/j.1551-2916.2009.03558.x (2010).
- 57 Liu, Xiang Zheng, Man Chun Xie, Kai, Mechanism of lithium storage in Si-O-C composite anodes, *Journal of Power Sources* **196**, 10667-10672 (2011)
- 58 Mutin, P. H. Control of the composition and structure of silicon oxycarbide and oxynitride glasses derived from polysiloxane precursors. *Journal of Sol-Gel Science and Technology* **14**, 27-38, doi:10.1023/a:1008769913083 (1999).
- 59 Sanchez-Jimenez, P. E. & Raj, R. Lithium Insertion in Polymer-Derived Silicon Oxycarbide Ceramics. *Journal of the American Ceramic Society* **93**, 1127-1135, doi:10.1111/j.1551-2916.2009.03539.x (2010).
- 60 Singh, A. K. & Pantano, C. G. Surface chemistry and structure of silicon oxycarbide gels and glasses. *Journal of Sol-Gel Science and Technology* **8**, 371-376, doi:10.1007/bf02436867 (1997).
- 61 Soraru, G. D., Liu, Q., Interrante, L. V. & Apple, T. Role of precursor molecular structure on the microstructure and high temperature stability of silicon oxycarbide glasses derived from methylene-bridged polycarbosilanes. *Chemistry of Materials* **10**, 4047-4054, doi:10.1021/cm9804719 (1998).
- 62 Soraru, G. D. *et al.* Chemical durability of silicon oxycarbide glasses. *Journal of the American Ceramic Society* **85**, 1529-1536 (2002).
- 63 Xu, T., Ma, Q. & Chen, Z. High-temperature behavior of silicon oxycarbide glasses in

- air environment. *Ceramics International* **37**, 2555-2559, doi:10.1016/j.ceramint.2011.03.053 (2011).
- 64 Xu, T., Ma, Q. & Chen, Z. The effect of environment pressure on high temperature stability of silicon oxycarbide glasses derived from polysiloxane. *Materials Letters* **65**, 1538-1541, doi:10.1016/j.matlet.2011.02.065 (2011).
- 65 Ahn, D. & Raj, R. Thermodynamic measurements pertaining to the hysteretic intercalation of lithium in polymer-derived silicon oxycarbide. *Journal of Power Sources* **195**, 3900-3906, doi:10.1016/j.jpowsour.2009.12.116 (2010).
- 66 Rui, X., Yan, Q., Skyllas-Kazacos, M., & Lim, T. M. (2014). Li<sub>3</sub>V<sub>2</sub>(PO<sub>4</sub>)<sub>3</sub> cathode materials for lithium-ion batteries: A review. *Journal of Power Sources*, 258, 19- 38.
- 67 Etacheri, V., Marom, R., Elazari, R., Salitra, G. & Aurbach, D. Challenges in the development of advanced Li-ion batteries: a review. *Energy & Environmental Science* **4**, 3243-3262, doi:10.1039/c1ee01598b (2011).

## Chapter 3 - Processing of TiO<sub>2</sub>- SiOC

### 3.1 Introduction

Polymer derived ceramics (PDCs) tested for electrochemical applications have shown to have significantly higher capacities (700 mAh/g) compared to conventional graphite electrodes (300mAh/g). However, they usually lack durability due to their glassy nature, with degradation in performance after about 30 cycles. A study by Raj and Behera [2] has shown a compound ceramic of TiO<sub>2</sub> (10%) infused in SiOC to have a consistently high cycling capacity of about 900 mAh/g for more than 300 cycles at high current ratings. The aim of this research is to confirm the findings and to explore the material further by studying the effect of various ratios of TiO<sub>2</sub> nano – particles (30% and 50%) in the ceramic. There can be various polymers that can be processed to form ceramics as shown in Figure 33. We will be using 1,3,5,7 – tetra vinyl – 1,3,5,7 -tetra tetramethylcyclotetrasiloxane (TTCS) as the polymer to obtain the final silicon oxy carbide ceramic.

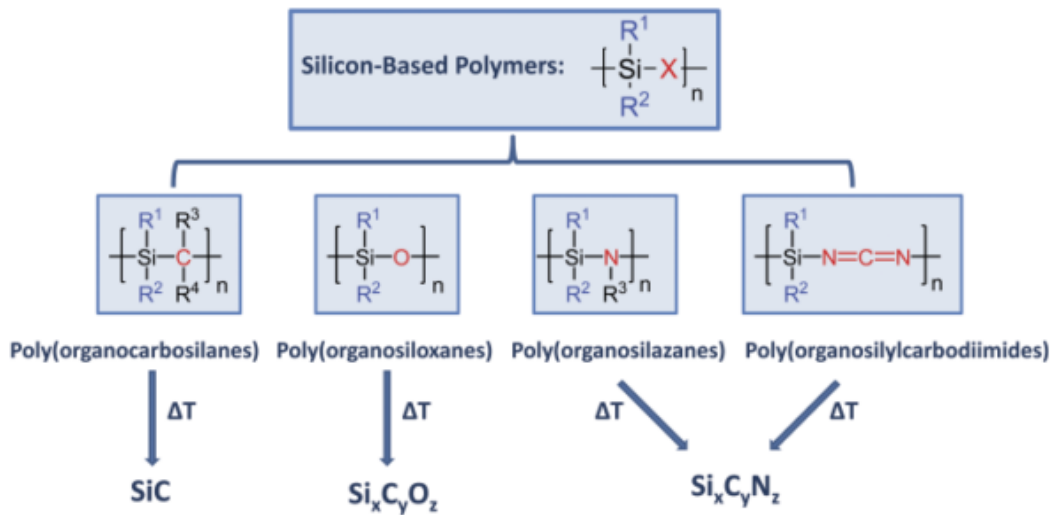


Figure 33 Thermal decomposition methods for silicon-based polymers [5]

### 3.2 Experimental Procedure

The material samples were prepared so as to have 10%, 30% and 50% by weight, of TiO<sub>2</sub> (100% anatase phase) with 15 nm average particle size and the remainder being a solution of 1,3,5,7-tetravinyl-1,3,5,7-tetramethylcyclotetrasiloxane (TTCS, Gelest, NJ, USA) with 1% dicumyl peroxide, which is the radical initiator. TiO<sub>2</sub> nanoparticles were slowly dropped into the TTCS solution with mechanical agitation, followed by stirring at about 300 rpm for about 24 hours to create a homogeneous dispersion. The mixture was then slowly dried in an inert atmosphere at 80 °C, which facilitates evaporation of the organic byproducts formed during the reaction. The dried powder was then cross-linked at 200 °C for 4 hours and pyrolyzed at 1000°C for 4 hours, under argon flowing at approximately 25 mL/min. The heating rate for crosslinking was 10 °C/min while that for pyrolysis was 5 °C/min. For the samples prepared for different weight percentages of TiO<sub>2</sub> (10%, 30% and 50%), same material composition, heating/cooling rate and dwell times were used.

Figure 34 shows the material being put in for cross –linking. The major challenges during the process included working with fragile tubes and preventing mixture spillage while setting up the apparatus.



**Figure 34 Showing the material put in for cross-linking**

Care also had to be taken to wash the apparatus at least twice with ethanol after using detergents to prevent contamination of the final product. Figure 35 shows the complete cross – linking apparatus – the argon gas cylinders to the left, the gas input and output pipes, the cross linking flask, the oven and the bubble tube.



**Figure 35 Showing the complete cross linking apparatus**

The input and output ports in the setup had to be adjusted so as to have proper circulation of air in the main chamber while providing sufficient current to carry away the evolved gases from the cross – linking chemicals. Figure 36 shows the cross linking flask with the door of the oven open. The lid of the flask was clamped to the main tube using an aluminum clamp to make the setup air tight. The chemicals were mixed in a smaller bottle and placed at the bottom of the tube to prevent material contamination. The output port for gases was manually purged for about 15 minutes in order to remove any air from the setup, at a constant temperature of about 40 °C, after which the temperature was raised slowly to 200 °C for cross-linking after drying at 80 °C.



**Figure 36 Showing the input and output gas pipes in the cross linking apparatus**

After cross linking, the product was allowed to reach room temperature naturally. The cross linked product was a white solid agglomerated mass. This had to be crushed using a crystal mortar to very fine particles as the quality of the final cross – linked product was highly dependent on the size of these particles. This crushed cross linked polymer was then put in for pyrolysis. Figure 37 shows the crushed product and Figure 38 shows the material being put on a weighing paper to be weighed



**Figure 37 Crushed mixture to be put in for pyrolysis**

and eventually put in for pyrolysis.



**Figure 38 Mixture being prepared to be put in the pyrolysis oven after weighing**

The initial pyrolysis ramp rate was  $5^{\circ}\text{C}$  per minute taking the temperature from  $0^{\circ}\text{C}$  to  $1000^{\circ}\text{C}$  in 200 minutes. This temperature was maintained at  $1000^{\circ}\text{C}$  for about 60 minutes and this is the time when the pyrolysis and conversion of polymer to ceramic takes place. Figure 39 shows the pyrolysis oven being programmed and set up for the experiment.

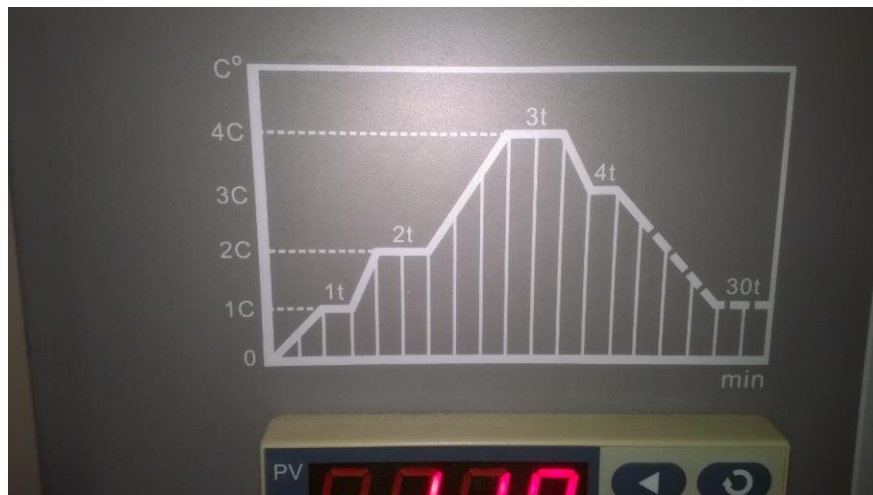


**Figure 39 Figure showing how the program for pyrolysis is set up**



The complete reaction takes place in an inert environment of ultra-high purity argon gas and the gases carried out in such a manner keep the relative pressure inside the chamber low so as to facilitate the evolution of by-product gases from cross – linked agent. Figure 40 shows the ceramic obtained after pyrolysis and Figure 41 shows the ceramic boat which contained the cross linked product for pyrolysis. The ceramic boat has to be heated in an inert environment up to 1000°C again in order to clean it properly for the next pyrolysis setup.



**Figure 40 Final product obtained after pyrolysis**



**Figure 41 Ceramic boat after material removal after pyrolysis**

The ceramic obtained after pyrolysis was then mixed with carbon black and 5% poly acrylic acid solution in N-Methyl-2-pyrrolidone (NMP) solution. The mixture contained 70% by weight of the ceramic with 15% by weight carbon black and 15% by weight the PAA-NMC solution, which acted as the binding agent.

Figure 42 shows the carbon black and PAA – NMC solution along with the dropper. And Figure 43 shows the mixture in a mortar pestle being mixed together and being crushed simultaneously. Care had to be taken while weighing the PAA solution using a dropper and about 4 to 5 drops of NMC had to be added to the mixture in the mortar pestle to facilitate mixing and obtain the desired consistency, as learnt by experience. Care also had to be taken to limit the area of mixing to a small region to prevent wastage of the material.

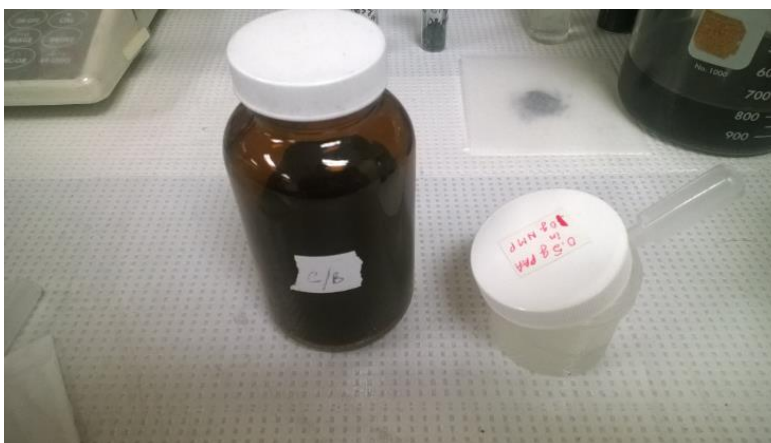


**Figure 42 Carbon black and binding agent for electrode coating**



**Figure 43 Mixing the pyrolyzed material with binder**

Figure 44 shows the copper foil being cut, clamped and prepared for application on a glass slate.

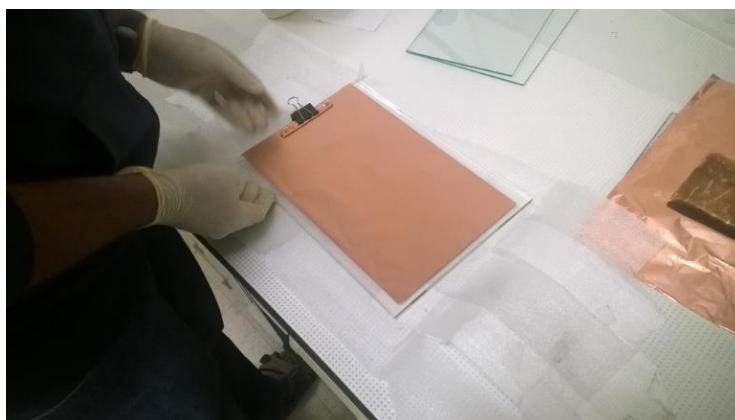


**Figure 44 Clamping the copper foil on the glass slate**

The paste obtained was then spread on this copper foil to obtain a uniform thickness of 50 microns and the battery electrodes were punched out from this coated foil as shown in Figure 45.



**Figure 45 Coating the copper foil using the doctor blade method**

## References

1. Ahn, D. & Raj, R. Cyclic stability and C-rate performance of amorphous silicon and carbon based anodes for electrochemical storage of lithium. *Journal of Power Sources* **196**, 2179-2186, doi:10.1016/j.jpowsour.2010.09.086 (2011).
2. Behera, S. K. & Raj, R. Extreme-rate capable and highly stable SiCO-TiO<sub>2</sub> hybrids for Li ion battery anodes. *Chemical Communications* **49**, 9657-9659, doi:10.1039/c3cc45311a (2013).
3. Morales-Garcia, A. *et al.* First-principles study of structure and stability in Si-C-O-based materials. *Theoretical Chemistry Accounts* **132**, doi:10.1007/s00214-012-1308-6 (2013).
4. Tomar, V., Gan, M. & Kim, H. S. Atomistic analyses of the effect of temperature and

- morphology on mechanical strength of Si-C-N and Si-C-O nanocomposites. *Journal of the European Ceramic Society* **30**, 2223-2237, doi:10.1016/j.jeurceramsoc.2010.03.002 (2010).
5. Colombo, P., Mera, G., Riedel, R. & Soraru, G. D. Polymer-Derived Ceramics: 40 Years of Research and Innovation in Advanced Ceramics. *Journal of the American Ceramic Society* **93**, 1805-1837, doi:10.1111/j.1551-2916.2010.03876.x (2010).
  6. Liu, Xiang Zheng, Man Chun Xie, Kai, Mechanism of lithium storage in Si-O-C composite anodes, *Journal of Power Sources* **196**, 10667-10672 (2011)
  7. Sanchez-Jimenez, P. E. & Raj, R. Lithium Insertion in Polymer-Derived Silicon Oxycarbide Ceramics. *Journal of the American Ceramic Society* **93**, 1127-1135, doi:10.1111/j.1551-2916.2009.03539.x (2010).
  8. Ahn, D. & Raj, R. Thermodynamic measurements pertaining to the hysteretic intercalation of lithium in polymer-derived silicon oxycarbide. *Journal of Power Sources* **195**, 3900-3906, doi:10.1016/j.jpowsour.2009.12.116 (2010).

## Chapter 4 - Characterization of TiO<sub>2</sub> – SiOC

### 4.1 Scanning Electron Microscopy

Scanning electron microscopy can be used for structural and chemical characterization of nano-materials. This technology has an electron beam which scans on the sample just like a cathode ray tube in a television scans the screen. The energy of the electrons determines the kind of image and the depth of the sample being imaged. Low energy beams scan the surface while higher energy beams can be used to image the depths of the sample. Many factors determine the energy of the electrons, like the length of the SEM chamber, the filament material (work function), the tip size of the filament, etc. The SEM used was Carl Zeiss EVO Low-Vacuum SEM and Figure 46 shows the schematic and software screen shots of the scanning electron microscope which was used during our analysis.

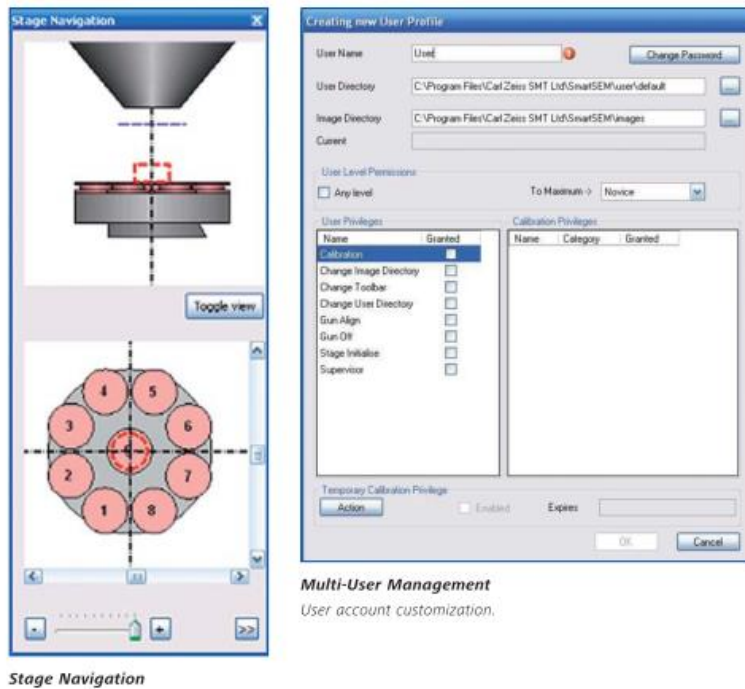
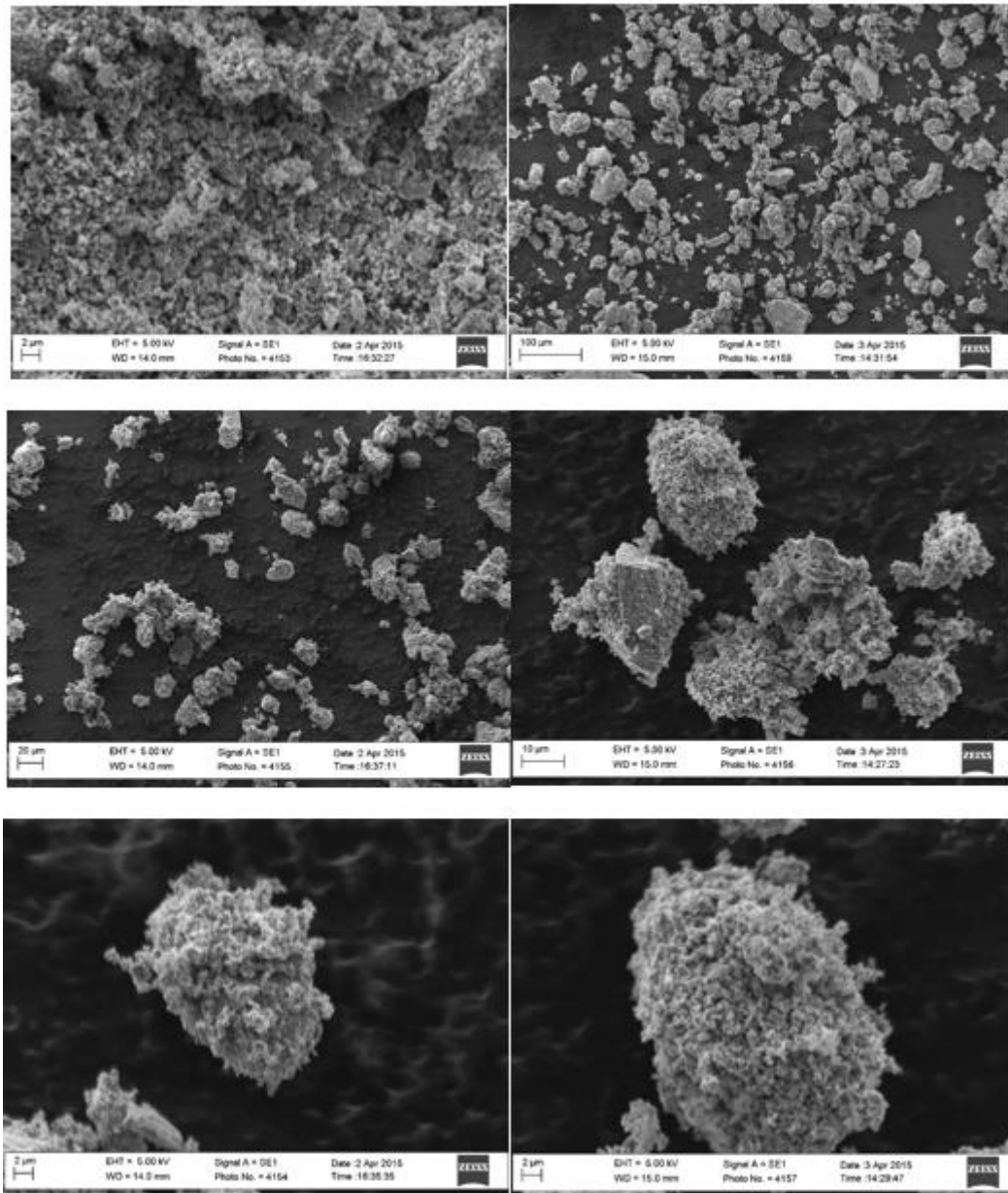


Figure 46 Screenshots of the SEM used during our analysis

Figure 47 shows the SEM images of the sample. The image captures the ceramic material from different depths of focus with larger ceramic particles ranging from 5  $\mu\text{m}$  to 20  $\mu\text{m}$  with the 5kV electron accelerating voltage and magnifications of more than 3400x. Figure 48 (a) and (b) show



**Figure 47 Showing the SEM imaging of the sample**

the SEM images taken for pre-cycling and post-cycling as taken from reference 1. As can be seen from the SEM images in Figure 47, the morphology of the particles suggest an amorphous outer surface, which is what should be expected for the material processed at 1000° C.

The material was crushed manually using a mortar pestle and hence the size and structure of the particles depend on the time, effort and technique used for crushing them as well. The images obtained show that the particles are fairly conducting to electrons, as there is no localized accumulation of electrons on the surface.

Figure 48 (c) and (d) show the proposed model for the ceramic for different processing temperatures. The proposed model based on pre-cycling and post-cycling images suggests a structure having a denser TiO<sub>2</sub> core, with an amorphous outer shell, which could be free carbon networks mixed with SiOC ceramic. Our SEM images of the outer surface seem to agree well with the proposed model. We would be using TEM to determine the structure characteristics at the core as documented in the next section.

## **4.2 Transmission Electron Microscopy**

Transmission electron microscopy creates an image on a fluorescent screen or a detector through the interaction of the electron beam, which is transmitted through a given specimen, and is magnified and focused. The image obtained depends on the energy of the electrons just like in SEM.

Raj and Behera [1] conducted similar experiments and proposed the ceramic structure shown in Figures 48 – (c) and (d), for the ceramic processed at 600° C (crystalline) and 800° C (amorphous)



respectively. Images (a), and (b), are SEM images of the ceramic before cycling and after 3000 charge – discharge cycles.

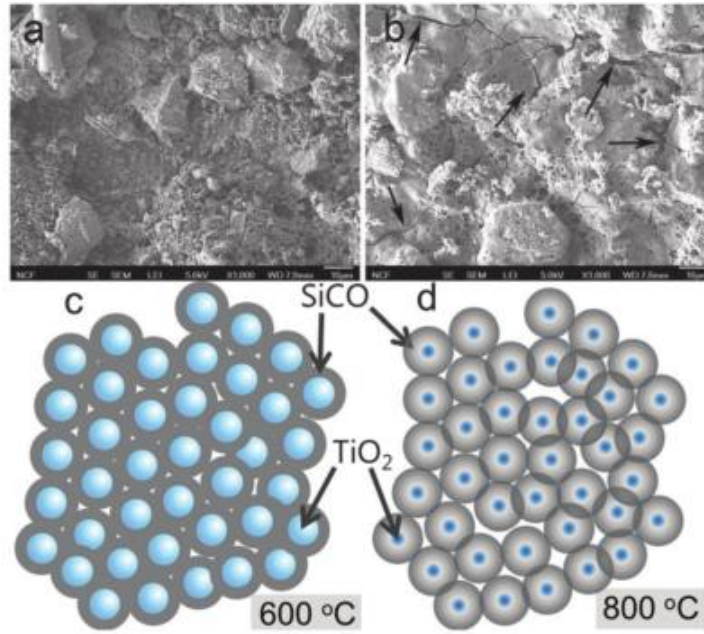


**Figure 48 (a) SEM image of sample, (b) SEM image after cycling, (c) and (d) Proposed ceramic structure at 600° and 800° C[1]**

The specimen for TEM was collected on a 50 mesh copper grid with a thin carbon membrane and was inserted into the TEM. Figure 49 shows the TEM images of the sample. It can be clearly seen from the images that there exists a concentrated core in the material with less dense outer regions. As mentioned above, these can be hypothesized as concentrated cores of  $\text{TiO}_2$  surrounded by less dense and amorphous, carbon rich SiOC.

Figure 49 (a) shows the TEM image of  $\text{TiO}_2$  nano particles only. They look agglomerated in the

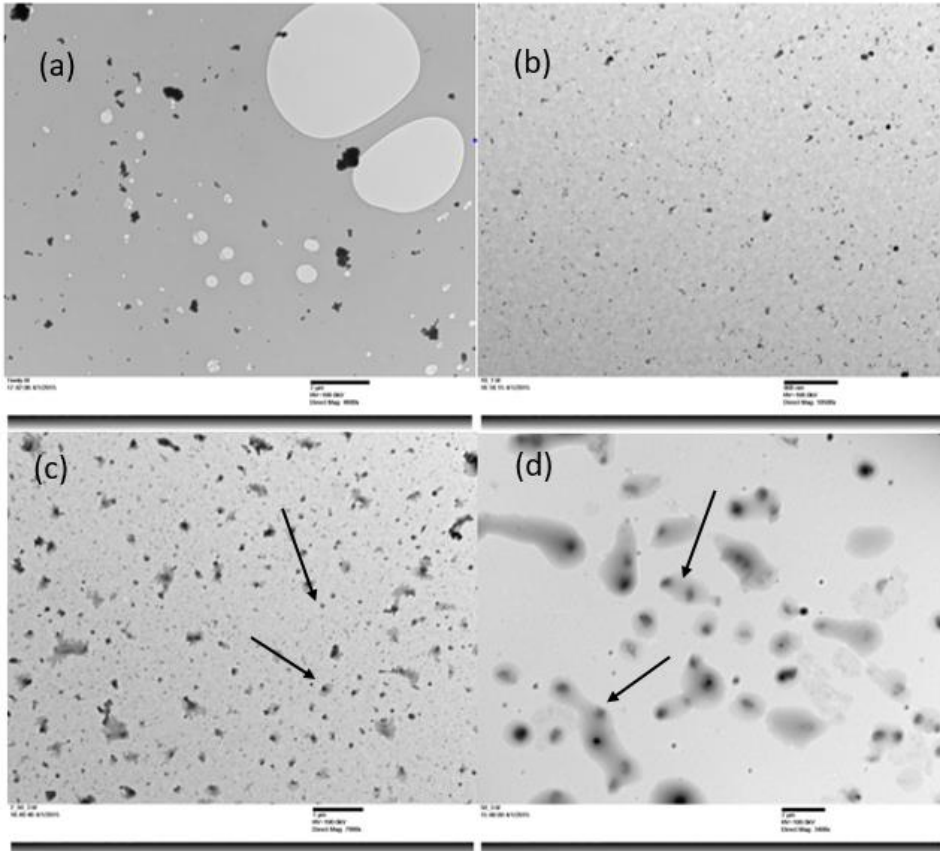


**Figure 49 TEM images of – (a) TiO<sub>2</sub> only, (b) 10% sample, (c) 30% sample, (d) 50% sample**

TEM image above, which could be due to wetting when preparing the TEM grid. As can be clearly observed from Figures 49 (b), (c), and (d), the size and structure of the ceramic is dictated by the amount of TiO<sub>2</sub> present in the sample. The TiO<sub>2</sub> particles are providing sites of seeding and the number density of particles in a particular area is highest for the 50% sample, intermediate for the 30% sample and the least for the 10% sample as should be expected. The SEM and TEM results thus obtained, seem to correspond very well with the proposed model in figure 49. The arrows in the figure indicate the denser and possibly crystalline, TiO<sub>2</sub> cores with less dense outer regions which should be carbon rich SiOC. We conducted FTIR and XRD as documented in the next two sections to investigate the material further.

### 4.3 Fourier Transform infrared spectroscopy

Fourier transform infrared spectroscopy is a technique which is used to determine the sample chemical composition, usually for identifying the covalent bonds in the material. Ionic compounds are generally transparent to the infrared rays used for the analysis, while the transmittance for covalent compounds is recorded and Fourier transformed graph is plotted. Figure 50 shows the instruments used for the FTIR analysis.



**Figure 50 Instruments used for FTIR**

The wavelength of the radiation absorbed is related to the strength of the covalent bond which makes identifying hydrogen, covalent,  $sp^2$  and  $sp^3$  bonds possible. Figure 51 shows the FTIR plot of the ceramic.

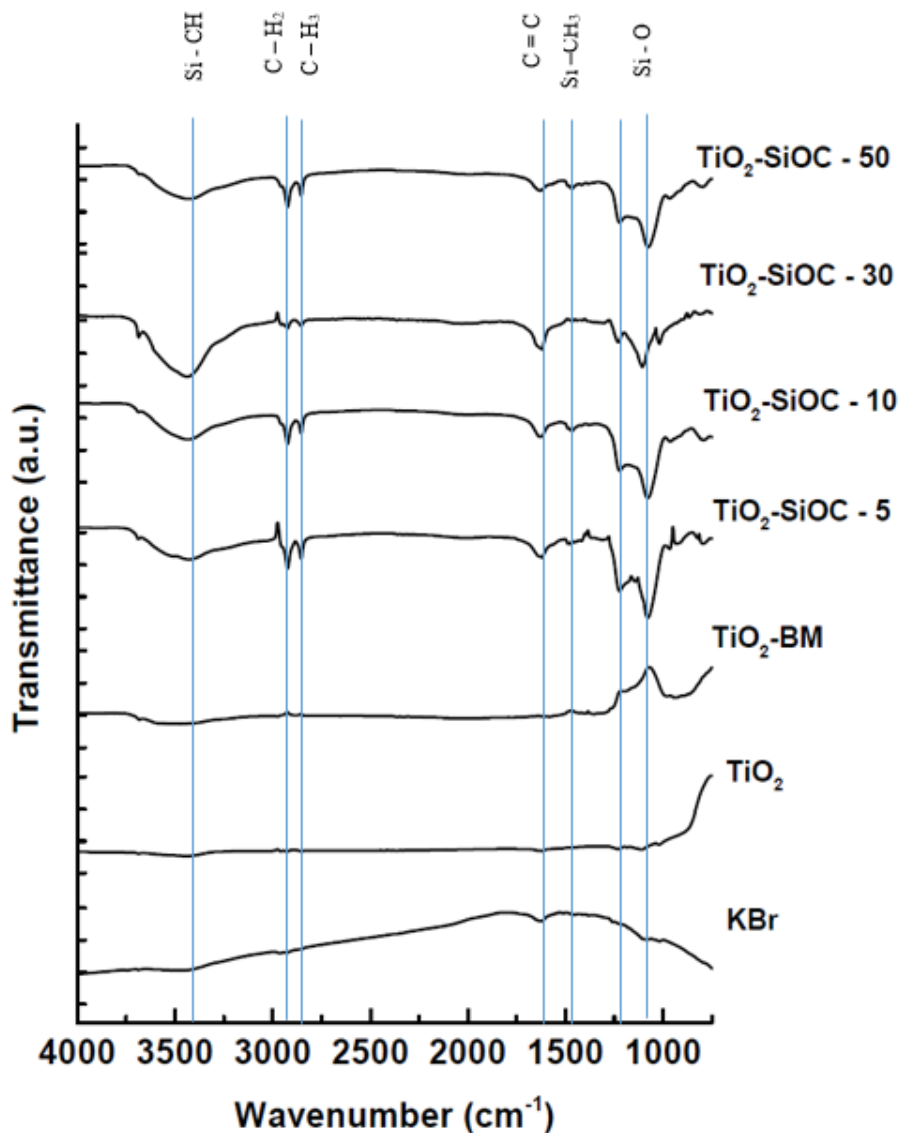


**Figure 51 FTIR measurements of the different samples**

The material is characterized by mixing it 1% by weight in an ionic compound like KBr, which is transparent to the infrared radiation. TiO<sub>2</sub>, which is an ionic compound is also transparent to the infrared rays. There are Si-CH bonds observed at around 3400  $cm^{-1}$ . C-H bonds can be observed

at  $2800\text{ cm}^{-1}$  and  $2700\text{ cm}^{-1}$ , corresponding to  $sp^2$  and  $sp^3$  carbon respectively. The C=C bond can be observed around  $1700\text{ cm}^{-1}$  and the Si-O bond is very prominent at around  $1200\text{ cm}^{-1}$ . This spectrum is very identical to the SiOC spectrum and hence it can be concluded that the cross linking and pyrolysis of the  $\text{TiO}_2$  – TTCS mix lead to the formation of carbon rich SiOC, which mostly consist of the amorphous outer regions observed in the TEM and SEM images in the previous sections. XRD was then conducted to determine the crystal structure of the core.

#### 4.4 X- Ray Diffraction

X –Ray diffraction is used in order to determine the phase and the crystalline nature of the material specimen and also the unit cell type and dimensions. The figures below show the images of the XRD experiment. A Bruker powder X-Ray diffractometer using Cu –  $K\alpha$  radiation and nickel filter was used. The slit dimensions and initial angle of the detector are adjusted according to the final plot that is required.



**Figure 52 Instruments for XRD**

Figure 53 shows the XRD plots of the material. As can be seen, the three ceramic samples are amorphous in nature, just as the ball-milled sample of  $\text{TiO}_2$ . The original sample of  $\text{TiO}_2$  shows three peaks, the  $2\theta$  peaks for which correspond to  $27^\circ$ ,  $34^\circ$ , and  $38^\circ$ , confirm the anatase phase of the  $\text{TiO}_2$  which was initially mixed with the polymer. After pyrolysis, the final ceramic exhibits only amorphous nature. As discussed in reference 1, the structure of the ceramic depends on the

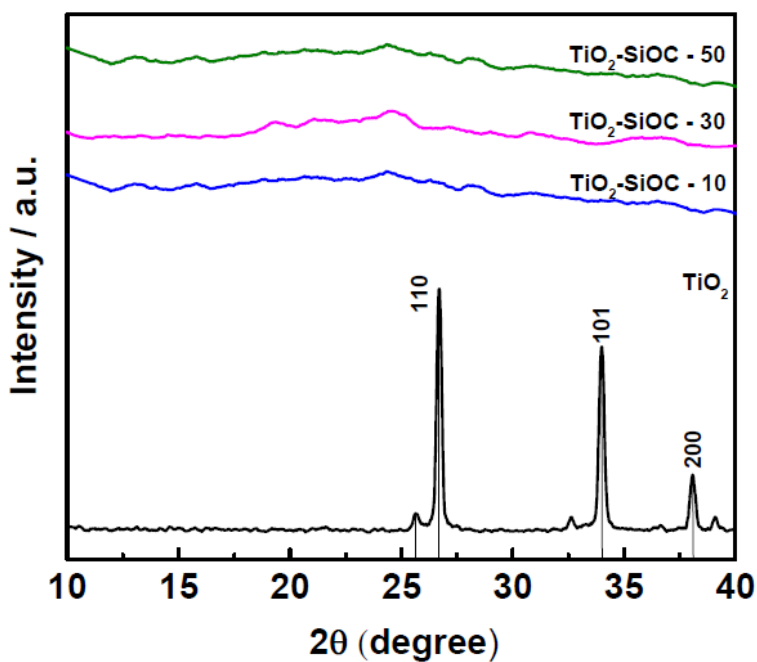


Figure 53 XRD plots of the samples

pyrolysis temperature and becomes more amorphous with higher temperatures. Here the pyrolysis temperature is  $1000^\circ\text{C}$  and the structure is amorphous as expected. Some degree of crystallinity can be expected when the temperatures are as low as  $600^\circ\text{C}$ .

#### 4.5 Raman Spectroscopy

Raman spectroscopy is a technique which is used to examine the structural evolution of the “free” carbon phase in PDC specimen. The wavelength of the radiations used in Raman spectroscopy are in or near the infrared regions. The energy of the photons in these radiations are transmitted directly to the molecules in the specimen. When they coincide with the vibrational energy modes of the molecule, resonance takes place, leading to amplified signals which can be detected and plotted. The covalent bonds may have three vibrational degrees of freedom, translational and rotational.

The Raman data can be used to distinguish between the  $sp^3$  band (D-band or the “defect-band”) and graphite-like  $sp^2$  band (G-band or the “graphite band”). Free carbon appears in the Raman spectra of PDCs in the form of disorder-induced D band at  $1350\text{ cm}^{-1}$  and, the G band at  $1582\text{ cm}^{-1}$  due to in- plane bond stretching of  $sp^2$ -hybridized carbon pairs. These two bands are significant features of disordered graphite-like carbon. The D-band becomes Raman active only through the existence of local disorder. On the other hand, the G-band is active at all  $sp^2$ -sites [3].

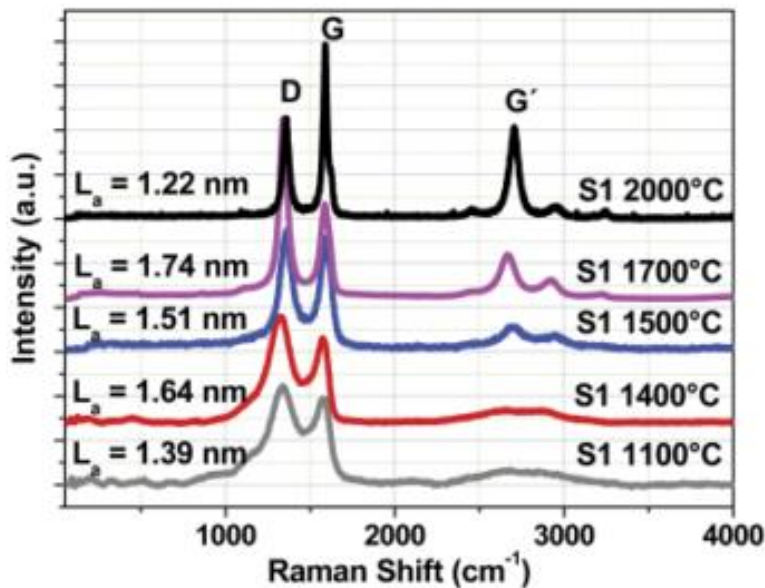


**Figure 54 Raman spectroscopy of silicon oxy carbide**

The instrument used for Raman spectroscopy was a Thermo Scientific DXR Raman microscope and an air-cooled green Nd:YAG laser ( $\lambda = 532 \text{ nm}$ ) of 5 mW power was used as excitation source. Spectra were collected on the instrument operating with 3.1  $\mu\text{m}$  confocal hole size, 50  $\mu\text{m}$  wide entrance slit, 900 grating lines/mm and 10X MPlan objective Olympus lens and data processing was performed using Thermo Scientific's Omnic software for microRaman.

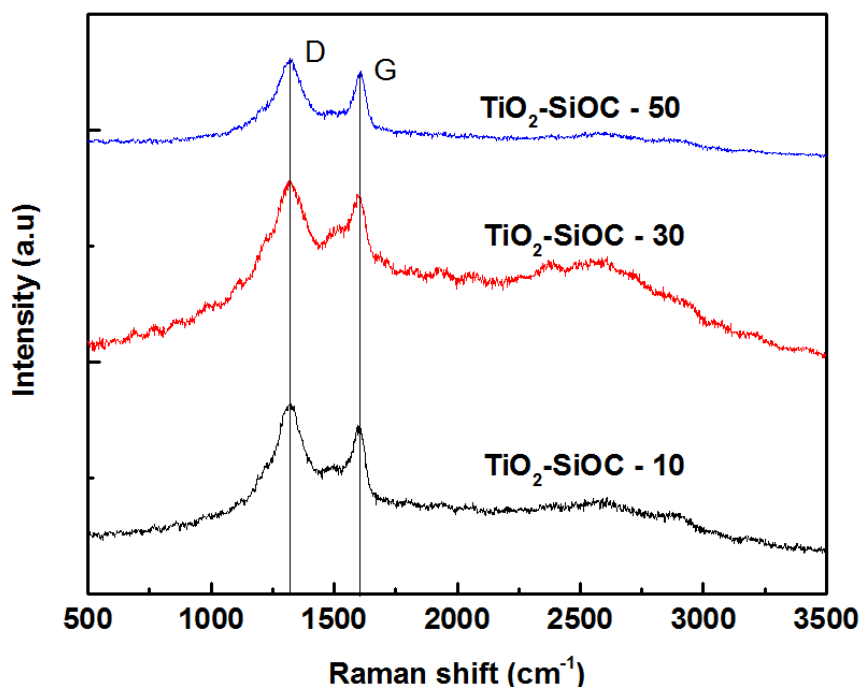


**Figure 55 Raman plots of the three samples**

The Raman spectra for the ceramic displayed peaks around  $1350 \text{ cm}^{-1}$  (D band) and  $1580 \text{ cm}^{-1}$  (G band) as shown in the above figure. The ratio of the D band peak to the G band peak is 1.12 in the 10% sample, 1.06 in the 30% sample and 1.13 in the 50% sample. As the D peak corresponds to  $\text{sp}^3$  carbon atoms and the G peak corresponds to  $\text{sp}^2$  carbon atoms, it can be concluded that the 30% sample has the highest ratio of the graphitic form of carbon and the 50% sample has the



highest ratio of the disordered diamond like  $sp^3$  carbon atoms. This has direct implications on the electronic conductivity and capacity of the specimens.

We cannot make any conclusive evidence of all the chemical reactions have taken place, especially with respect to the  $TiO_2$  particles, based on the SEM, TEM, XRD, FTIR and Raman analysis, except concluding about the size, structure, amorphous nature, effect of varying percentages of  $TiO_2$  nanoparticles on the above, and the presence of SiOC ceramic in the samples as was discussed in the various sections of this chapter, and further chemical analysis techniques like Nuclear Magnetic Resonance (NMR) and energy dispersive X – ray spectroscopy (EDX) might be required to analyze in more detail, how the  $TiO_2$  particles are reacting with the polymer during cross linking and pyrolysis. Our analysis indicates that the hypothesis about the ceramic model by Raj and Behera seems to be agreeing quite well with the results we obtained and hence we would base our future discussions on the proposed model from here onwards.

## References

1. Behera, S. K. & Raj, R. Extreme-rate capable and highly stable SiCO-TiO<sub>2</sub> hybrids for Li ion battery anodes. *Chemical Communications* **49**, 9657-9659, doi:10.1039/c3cc45311a (2013).
2. Bhandavat, R. & Singh, G. Stable and Efficient Li-Ion Battery Anodes Prepared from Polymer-Derived Silicon Oxycarbide-Carbon Nanotube Shell/Core Composites. *Journal of Physical Chemistry C* **117**, 11899-11905, doi:10.1021/jp310733b (2013).
3. Erdem, E. *et al.* Defect structure in lithium-doped polymer-derived SiCN ceramics

characterized by Raman and electron paramagnetic resonance spectroscopy. *Physical Chemistry Chemical Physics* **11**, 5628-5633, doi:10.1039/b822457a (2009).

4. Mera, G., Tamayo, A., Nguyen, H., Sen, S. & Riedel, R. Nanodomain Structure of Carbon-Rich Silicon Carbonitride Polymer-Derived Ceramics. *Journal of the American Ceramic Society* **93**, 1169-1175, doi:10.1111/j.1551-2916.2009.03558.x (2010).
5. Colombo, P., Mera, G., Riedel, R. & Soraru, G. D. Polymer-Derived Ceramics: 40 Years of Research and Innovation in Advanced Ceramics. *Journal of the American Ceramic Society* **93**, 1805-1837, doi:10.1111/j.1551-2916.2010.03876.x (2010).

## Chapter 5 - Electrochemical Performance of TiO<sub>2</sub> – SiOC

The cells were assembled in a glove box and cycled in a battery test rig at varying C- rates for a specified number of cycles. The C- rate was continuously increased from 1C to 24C in steps of 5 cycles each and then again brought back to 1C. This was done to test the mechanical strength and rate capability of the electrodes. The battery performance shot back up to around 100% capacity after the current loading was brought back to normal, which displayed that the electrode was capable of handling high currents. The batteries performed very well for a number of cycles, more than 450 cycles for the best performing sample as shown in Figure 56 below.

Galvanostatic charge–discharge cycling was carried out between the 0.01 and 2.5 V window. The curves in Figure 56 show the first cycle capacity loss in the battery after the first charge and discharge cycle. The active material in the anode weighed 3.07mg in the 10% cell, 2.44mg in the 30% cell and 3.11 mg in the 50% cell. The specific charge and discharge capacities are calculated with respect to the weight of the TiO<sub>2</sub> – SiCO hybrid ceramic material in the anodes. The first insertion cycle capacity for the SiCO–TiO<sub>2</sub> anodes, at a current density of 142.5 mA g<sup>-1</sup>,

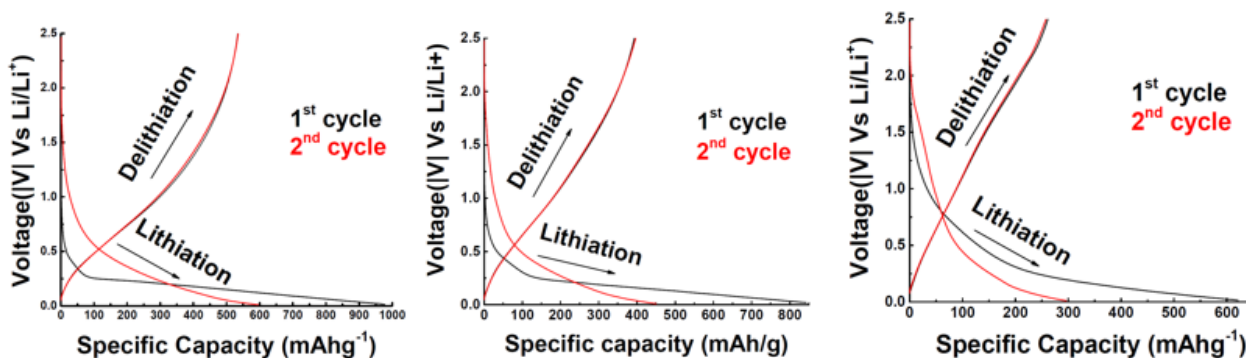
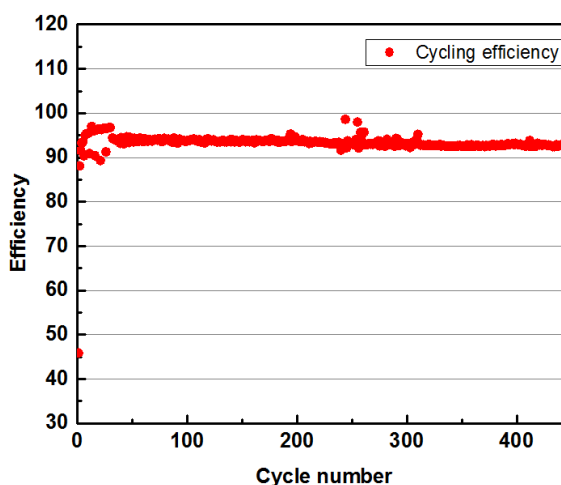


Figure 56 Showing the first cycle charge and discharge of the batteries

showed a specific capacity of 976 mAh g<sup>-1</sup>, 858 mAh g<sup>-1</sup> and 621 mAh g<sup>-1</sup> and the first extraction cycle showed a capacity of 595 mAh g<sup>-1</sup>, 450 mAh g<sup>-1</sup> and 296 mAh g<sup>-1</sup>, indicating the irreversible capacity loss (ICL) to be 39%, 47.5% and 52.17% for the 10%, 30% and 50% ceramics respectively. Figure 57 shows the cycling efficiency of the 30% sample while Table 1 gives a summary of the capacities and capacity losses for the first two cycles, The specific capacity values are similar to those observed in of polymer-derived bulk SiOC powders but the ICL observed is considerably higher, which is typically 33%. The coulombic efficiency was greater than 90% for the subsequent cycles.



**Figure 57 Cycling efficiency of the 30% sample**

**Table 1 Summary of electrochemical performance for two cycles**

<b>Sample</b>	<b>1<sup>st</sup> cycle discharge (mAhg<sup>-1</sup>)</b>	<b>1<sup>st</sup> cycle charge (mAhg<sup>-1</sup>)</b>	<b>2<sup>nd</sup> cycle discharge (mAhg<sup>-1</sup>)</b>	<b>2<sup>nd</sup> cycle charge (mAhg<sup>-1</sup>)</b>	<b>1<sup>st</sup> cycle efficiency loss</b>
<b>TiO<sub>2</sub>-SiOC- 10</b>	<b>977</b>	<b>533</b>	<b>596</b>	<b>535</b>	<b>39%</b>
<b>TiO<sub>2</sub>-SiOC- 30</b>	<b>858</b>	<b>393</b>	<b>450</b>	<b>396</b>	<b>47.5%</b>
<b>TiO<sub>2</sub>-SiOC- 50</b>	<b>621</b>	<b>261</b>	<b>297</b>	<b>258</b>	<b>52.17%</b>

The differential specific capacity curve in Figure 58 shows that most of the Li insertion occurred between 0.1 and 1 V, whereas Li extraction was spread over the full voltage window of 2.5 V, which is what is generally observed for SiOC electrodes. The nature of the curves determine whether the reaction taking place in the electrode is an intercalation reaction, or alloying or conversion reaction. Here the curves are smooth with peaks only at the lowest region of the differential capacity curve and hence this is a lithium intercalation reaction, which is what is expected in SiOC ceramics.

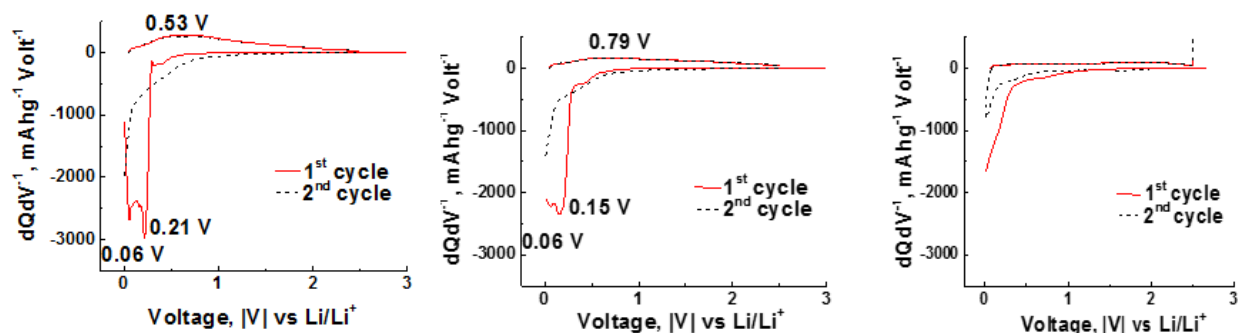


**Figure 58 showing the first cycle performance of the batteries**

The cells exhibited good cyclic stability during cycling. After the first 5 cycles at  $142.5 \text{ mA g}^{-1}$ , the current density was ramped up to  $285 \text{ mA g}^{-1}$ ,  $470 \text{ mA g}^{-1}$ ,  $940 \text{ mA g}^{-1}$ ,  $1880 \text{ mA g}^{-1}$  and  $3420 \text{ mA g}^{-1}$  for 5 cycles each and then brought back to  $142.5 \text{ mA g}^{-1}$ . In all the stages, the cells showed good cyclability and complete recovery of the inserted Li ions over many cycles was observed as shown in Figure 59. The figure shows cycling for the 30% ceramic, which was the best performing ceramic and cycled stably for over 450 cycles. When the cell was brought back to  $142.5 \text{ mA g}^{-1}$ , which corresponds to 1C rate the specific capacity recovered back to  $435 \text{ mAh g}^{-1}$  as can be observed in Figure 60.

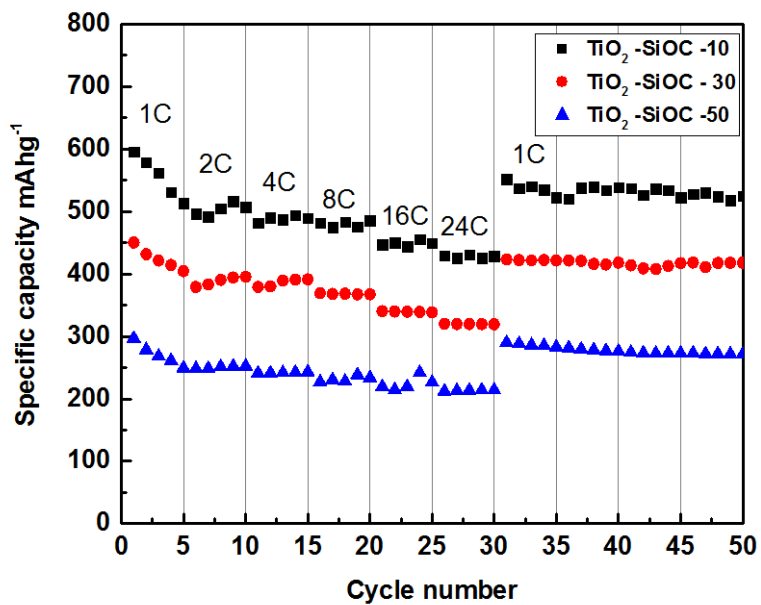


Figure 59 C-rate capability of the three anodes

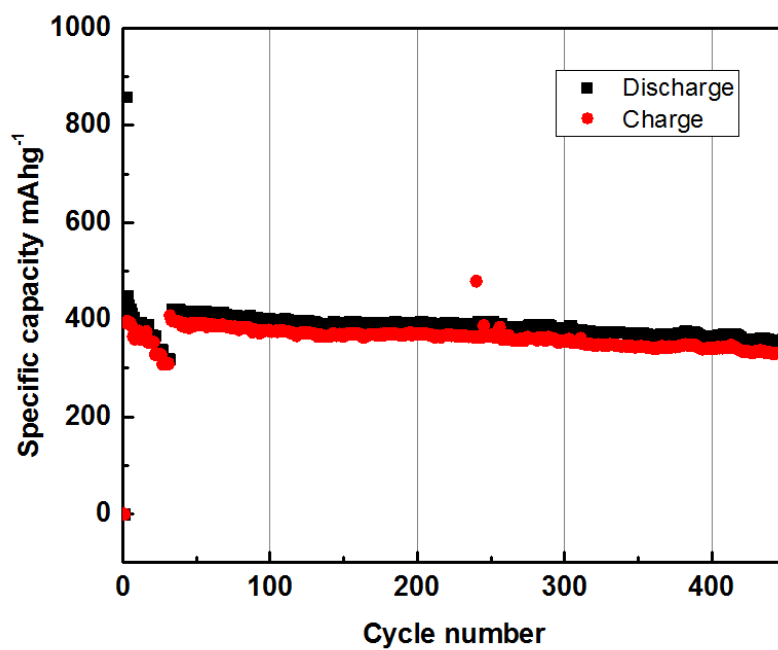


Figure 60 Charge – discharge cycling of the 30% sample

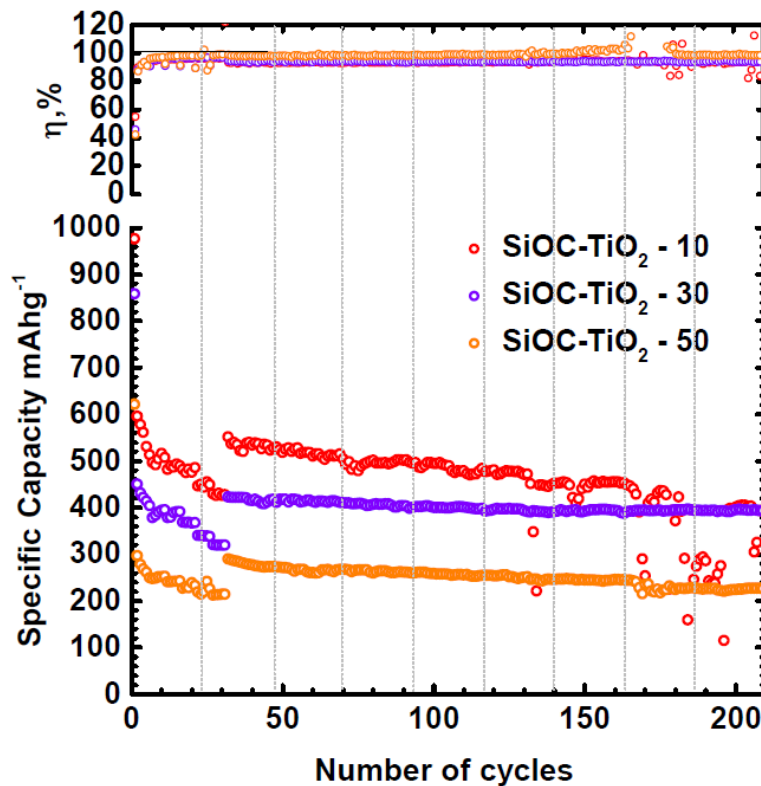


Figure 61 Showing the electrochemical cycling and cycling efficiency of the batteries

The lithium ions get intercalated at the sites of free carbon [6-10]. Figure 62 shows the domains of free carbon in SiOC ceramic and Figure 63 shows schematically, SiOC applied as a film on a

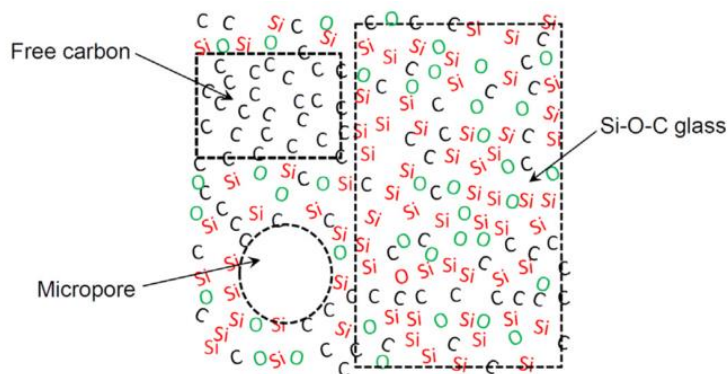
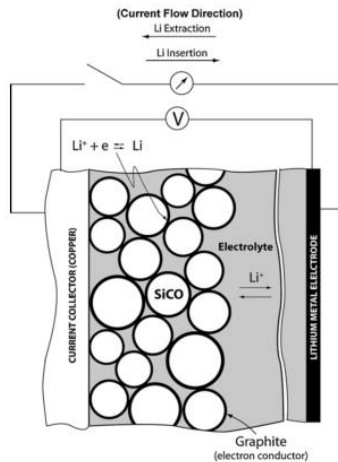


Figure 62 Schematic showing domains of free carbon and micropore in SiOC ceramic [13]



**Figure 63 Schematic representing the anode [11] -**

substrate. The SiOC –TiO<sub>2</sub> hybrid ceramic can be hypothesized as having a similar structure and adherence to the copper film. It can be observed that there are domains of micropores in the material along with domains of SiOC. There are mechanical fatigue stresses induced in the anode due to continuous cycling of the ions, which leads to eventual fracture due to the brittle nature of the ceramic.

In conclusion, the sample with 30% TiO<sub>2</sub> had the best overall performance with consistent capacities of around 450 mAhg<sup>-1</sup> for more than 450 cycles. A high first cycle capacity loss was observed for all three samples, and this was around 47.5% for the 30% sample. The mechanism of anode functioning was identified as intercalation mechanism from the differential capacity curves. Lithium insertion took place between 0.1 and 1V, and extraction was spread for the full voltage window of 2.5V. The cells exhibited good cycling performance with stable cycling at current densities as high as 24 C. The structure of the hybrid ceramic was hypothesized using references from existing literature and it was identified that eventual degradation in performance occurs due mechanical fracture due to stresses induced on continuous current cycling.



## References

- 1 Dibandjo, P., Graczyk-Zajac, M., Riedel, R., Pradeep, V. S. & Soraru, G. D. Lithium insertion into dense and porous carbon-rich polymer-derived SiOC ceramics. *Journal of the European Ceramic Society* **32**, 2495-2503, doi:10.1016/j.jeurceramsoc.2012.03.010 (2012).
- 2 Graczyk-Zajac, M., Mera, G., Kaspar, J. & Riedel, R. Electrochemical studies of carbon-rich polymer-derived SiCN ceramics as anode materials for lithium-ion batteries. *Journal of the European Ceramic Society* **30**, 3235-3243, doi:10.1016/j.jeurceramsoc.2010.07.010 (2010).
- 3 Kaspar, J., Graczyk-Zajac, M. & Riedel, R. Carbon-rich SiOC anodes for lithium-ion batteries: Part II. Role of thermal cross-linking. *Solid State Ionics* **225**, 527-531, doi:10.1016/j.ssi.2012.01.026 (2012).
- 4 Kaspar, J., Graczyk-Zajac, M. & Riedel, R. Lithium insertion into carbon-rich SiOC ceramics: Influence of pyrolysis temperature on electrochemical properties. *Journal of Power Sources* **244**, 450-455, doi:10.1016/j.jpowsour.2012.11.086 (2013).
- 5 Kaspar, J., Graczyk-Zajac, M. & Riedel, R. Determination of the chemical diffusion coefficient of Li-ions in carbon-rich silicon oxycarbide anodes by electro-analytical methods. *Electrochimica Acta* **115**, 665-670, doi:10.1016/j.electacta.2013.10.184 (2014).
- 6 Kaspar, J., Mera, G., Nowak, A. P., Graczyk-Zajac, M. & Riedel, R. Electrochemical study of lithium insertion into carbon-rich polymer-derived silicon carbonitride ceramics. *Electrochimica Acta* **56**, 174-182, doi:10.1016/j.electacta.2010.08.103 (2010).
- 7 Liu, X., Zheng, M.-C. & Xie, K. Mechanism of lithium storage in Si-O-C composite anodes. *Journal of Power Sources* **196**, 10667-10672,

- doi:10.1016/j.jpowsour.2011.08.072 (2011).
- 8 Pradeep, V. S., Graczyk-Zajac, M., Wilamowska, M., Riedel, R. & Soraru, G. D. Influence of pyrolysis atmosphere on the lithium storage properties of carbon-rich polymer derived SiOC ceramic anodes. *Solid State Ionics* **262**, 22-24, doi:10.1016/j.ssi.2013.08.043 (2014).
- 9 Pradeep, V. S., Graczyk-Zajac, M., Riedel, R. & Soraru, G. D. New Insights in to the Lithium Storage Mechanism in Polymer Derived SiOC Anode Materials. *Electrochimica Acta* **119**, 78-85, doi:10.1016/j.electacta.2013.12.037 (2014).
- 10 Reinold, L. M., Graczyk-Zajac, M., Gao, Y., Mera, G. & Riedel, R. Carbon-rich SiCN ceramics as high capacity/high stability anode material for lithium-ion batteries. *Journal of Power Sources* **236**, 224-229, doi:10.1016/j.jpowsour.2013.02.046 (2013).
- 11 Ahn, D. & Raj, R. Thermodynamic measurements pertaining to the hysteretic intercalation of lithium in polymer-derived silicon oxycarbide. *Journal of Power Sources* **195**, 3900-3906, doi:10.1016/j.jpowsour.2009.12.116 (2010).
- 12 Ionescu, E., Kleebe, H.-J. & Riedel, R. Silicon-containing polymer-derived ceramic nanocomposites (PDC-NCs): preparative approaches and properties. *Chemical Society Reviews* **41**, 5032-5052, doi:10.1039/c2cs15319j (2012).
- 13 Li, Y. *et al.* One-dimensional SiOC/C composite nanofibers as binder-free anodes for lithium-ion batteries. *Journal of Power Sources* **254**, 33-38, doi:10.1016/j.jpowsour.2013.12.044 (2014).

## Chapter 6 - Conclusion and Future Work

Thus we have demonstrated the use of titanium di-oxide infused silicon oxy-carbide as a potential anode material for lithium ion batteries. The material prepared was characterized using a number of topological and chemical techniques to study its structure and chemical composition. The batteries were assembled and cycled using a battery rig. It was found out that the battery anode with 30%  $\text{TiO}_2$  by composition performed the best among all the three samples as it had high capacity as well as good mechanical strength which performed well during cycling. The anode with 10%  $\text{TiO}_2$  demonstrated high conductivity and capacities, but dis-integrated after around 175 cycles, while the anode with 50%  $\text{TiO}_2$  had good cycling performance, but lacked in capacity.

The reasons for this difference in performance can be attributed to the quality and quantity of free graphene in the ceramics as well as the contribution of  $\text{TiO}_2$  nano particles to the mechanical strength of the anodes. The  $\text{TiO}_2$  nano-particles provide sites for carbon to grow in the form of graphene and the optimum composition was found to be around 30%  $\text{TiO}_2$  in the mixture.

In the future, our aim would be to do a post-electrochemical cycling study of the battery material. We also intend to study the effect of different temperatures on the material properties and study their electrochemical performance. Different chemical characterization techniques like NMR spectroscopy and EDX can also be used to examine the chemistry of the material further.